



A Short Gamma-Ray Burst from a Protomagnetar Remnant

N. Jordana-Mitjans¹, C. G. Mundell¹, C. Guidorzi^{2,3,4}, R. J. Smith⁵, E. Ramírez-Ruiz^{6,7}, B. D. Metzger^{8,9}, S. Kobayashi⁵, A. Gomboc¹⁰, I. A. Steele⁵, M. Shrestha⁵, M. Marongiu¹¹, A. Rossi¹², and B. Rothberg^{13,14}

¹Department of Physics, University of Bath, Claverton Down, Bath, BA2 7AY, UK; N.Jordana@bath.ac.uk

²Department of Physics and Earth Science, University of Ferrara, via Saragat 1, I-44122, Ferrara, Italy

³INFN—Sezione di Ferrara, Via Saragat 1, I-44122 Ferrara, Italy

⁴INAF—Osservatorio di Astrofisica e Scienza dello Spazio di Bologna, Via Piero Gobetti 101, I-40129 Bologna, Italy

⁵Astrophysics Research Institute, Liverpool John Moores University, 146 Brownlow Hill, Liverpool, L3 5RF, UK

⁶Department of Astronomy and Astrophysics, University of California, Santa Cruz, CA 95064, USA

⁷DARK, Niels Bohr Institute, University of Copenhagen, Jagtvej 128, DK-2200, Copenhagen, Denmark

⁸Columbia Astrophysics Laboratory, Columbia University, New York, NY 10027, USA

⁹Center for Computational Astrophysics, Flatiron Institute, New York, NY 10010, USA

¹⁰Center for Astrophysics and Cosmology, University of Nova Gorica, Vipavska 13, 5000 Nova Gorica, Slovenia

¹¹INAF—Osservatorio Astronomico di Cagliari, via della Scienza, 5-I-09047 Selargius, Italy

¹²INAF—Osservatorio di Astrofisica e Scienza dello Spazio, via Piero Gobetti 93/3, I-40129 Bologna, Italy

¹³LBT Observatory, University of Arizona, 933 N.Cherry Avenue, Tucson, AZ 85721, USA

¹⁴George Mason University, Department of Physics & Astronomy, MS 3F3, 4400 University Drive, Fairfax, VA 22030, USA

Received 2022 July 5; revised 2022 August 26; accepted 2022 September 22; published 2022 November 10

Abstract

The contemporaneous detection of gravitational waves and gamma rays from GW170817/GRB 170817A, followed by kilonova emission a day after, confirmed compact binary neutron star mergers as progenitors of short-duration gamma-ray bursts (GRBs) and cosmic sources of heavy r -process nuclei. However, the nature (and life span) of the merger remnant and the energy reservoir powering these bright gamma-ray flashes remains debated, while the first minutes after the merger are unexplored at optical wavelengths. Here, we report the earliest discovery of bright thermal optical emission associated with short GRB 180618A with extended gamma-ray emission—with ultraviolet and optical multicolor observations starting as soon as 1.4 minutes post-burst. The spectrum is consistent with a fast-fading afterglow and emerging thermal optical emission 15 minutes post-burst, which fades abruptly and chromatically (flux density $F_\nu \propto t^{-\alpha}$, $\alpha = 4.6 \pm 0.3$) just 35 minutes after the GRB. Our observations from gamma rays to optical wavelengths are consistent with a hot nebula expanding at relativistic speeds, powered by the plasma winds from a newborn, rapidly spinning and highly magnetized neutron star (i.e., a millisecond magnetar), whose rotational energy is released at a rate $L_{\text{th}} \propto t^{-(2.22 \pm 0.14)}$ to reheat the unbound merger-remnant material. These results suggest that such neutron stars can survive the collapse to a black hole on timescales much larger than a few hundred milliseconds after the merger and power the GRB itself through accretion. Bright thermal optical counterparts to binary merger gravitational wave sources may be common in future wide-field fast-cadence sky surveys.

Unified Astronomy Thesaurus concepts: [High energy astrophysics \(739\)](#); [Time domain astronomy \(2109\)](#); [Gamma-ray bursts \(629\)](#); [Magnetars \(992\)](#); [Polarimetry \(1278\)](#)

Supporting material: machine-readable table

1. Introduction

Gamma-ray bursts (GRBs) are bright extragalactic flashes of gamma-ray radiation and briefly the most energetic explosions in the universe (Gehrels et al. 2009). Their catastrophic origin—the merger of compact star binaries for short-duration GRBs (Paczynski 1986; Fryer et al. 1999; Lee & Ramirez-Ruiz 2007; Tanvir et al. 2013; Abbott et al. 2017b) or the collapse of massive stars for long GRBs (Woosley 1993; Bloom et al. 1999; MacFadyen & Woosley 1999)—drives the formation of a newborn compact remnant (black hole or magnetar) that powers two highly relativistic jets. In the framework of the standard fireball model and after the initial prompt gamma-ray emission (e.g., Mészáros & Rees 1997; Piran 1999), the relativistic ejecta are decelerated by the circumburst medium by

a pair of external shocks: a short-lived reverse shock and a forward shock (e.g., Rees & Meszaros 1992; Sari & Piran 1999; Kobayashi 2000). This lagging emission called the afterglow radiates via synchrotron emission and can be detected seconds to years after the burst at wavelengths across the electromagnetic spectrum (e.g., Costa et al. 1997; van Paradijs et al. 1997; Gehrels et al. 2009).

Short GRBs represent 9% of the total detected by the Swift Burst Alert Telescope (BAT; Lien et al. 2016), resulting in a significantly lower frequency of real-time multiwavelength studies when compared to long GRBs. Additionally, the optical counterparts of short GRBs are typically a few hundred times fainter than those of massive star collapse origin (Kann et al. 2011). This challenges the early follow-up and the study of short GRBs with small and medium-sized telescopes, and limits the available data to several hours post-burst, in the kilonovae time domain (Tanvir et al. 2013; Abbott et al. 2017a; Troja et al. 2018).

Successful broadband follow-up of short GRBs began with the discovery of the X-ray and optical afterglow of GRB



Original content from this work may be used under the terms of the [Creative Commons Attribution 4.0 licence](#). Any further distribution of this work must maintain attribution to the author(s) and the title of the work, journal citation and DOI.

050709 (Fox et al. 2005; Hjorth et al. 2005; Villasenor et al. 2005), and first radio afterglow of GRB 050724 (Berger et al. 2005). After these events, there have been numerous detections of short GRB afterglows (e.g., Fong et al. 2015), including the first detection of a kilonova (Berger et al. 2013; Tanvir et al. 2013) and the joint discovery of the GW170817/GRB 170817A/kilonova, which confirmed that binary neutron stars are progenitors of at least some short GRBs (Abbott et al. 2017a, 2017b; Goldstein et al. 2017; Tanvir et al. 2017). Still, the remnant of neutron star binary mergers remains largely debated (Murguia-Berthier et al. 2014, 2021; Ruiz & Shapiro 2017; Metzger et al. 2018; Margalit & Metzger 2019; Metzger 2019; Beznogov et al. 2020; Mösta et al. 2020). More recently, giant flares from extragalactic magnetars have been associated as sources of low-luminosity short-duration GRBs (Fermi-LAT Collaboration et al. 2021; Roberts et al. 2021; Svinkin et al. 2021).

Here, we present the early-time multiwavelength observations and polarization constraint of GRB 180618A, a short GRB with extended emission (e.g., Norris & Bonnell 2006). So far, the only polarization measurement of a short GRB optical counterpart has been the $P = 0.50\% \pm 0.07\%$ detection in the GW170817 kilonova at ≈ 1.5 days after the merger (Covino et al. 2017)—consistent with polarization from Galactic dust. Short GRBs with extended soft gamma-ray emission are rarely studied at lower frequencies (Perley et al. 2009; Knust et al. 2017), as they are a small fraction of the total detected by the BAT ($\approx 1\%$; Lien et al. 2016). Such elusive objects are merger candidates and display the typical short hard prompt gamma-ray emission followed by variable soft gamma-ray emission spanning 10–100 s (Norris & Bonnell 2006; Perley et al. 2009; Hu et al. 2014; Kaneko et al. 2015). Candidate mechanisms powering such extended gamma-ray emission after the merger include late-time activity from the central engine (Metzger et al. 2008; Bucciantini et al. 2012), interaction with a pulsar-wind cavity (Ramirez-Ruiz et al. 2019), prolonged accretion from the gravitationally bound material ejected premerger (Lee & Ramirez-Ruiz 2007; Rosswog 2007; Lee et al. 2009), or a two-component outflow viewed slightly off-axis (Barkov & Pozanenko 2011).

This work is structured as follows. In Section 2, we present the GRB 180618A optical observations and data reduction of the UltraViolet and Optical Telescope (UVOT) and the 2 m Liverpool Telescope (LT)—including the RINGO3 multi-wavelength polarimeter/imager and the IO:O camera. In addition, we detail the 8.4 m Large Binocular Telescope (LBT) observations; that is, deep-field imaging with the Large Binocular Cameras (LBC) and spectroscopy of the host galaxy candidates with the Multi-Object Double Spectrographs (MODS). In Section 3, the properties of the optical and gamma-ray emission are presented. In Section 4, the physical origin of the peculiar multiwavelength emission of GRB 180618A is discussed—in particular, the optical emission. In Section 5, the implications of the GRB 180618A results are discussed in the wide context of neutron star mergers. In Section 6, we summarize our findings.

We assume a flat Λ CDM cosmology with $\Omega_m = 0.32$, $\Omega_\Lambda = 0.68$, and $h = 0.67$, as reported by Planck Collaboration et al. (2020). We adopt the convention $F_\nu \propto t^{-\alpha} \nu^{-\beta}$, where α is the temporal index, and β is the spectral index. Note that the spectral index is related to the photon index like $\beta = \beta_{\text{PI}} - 1$.

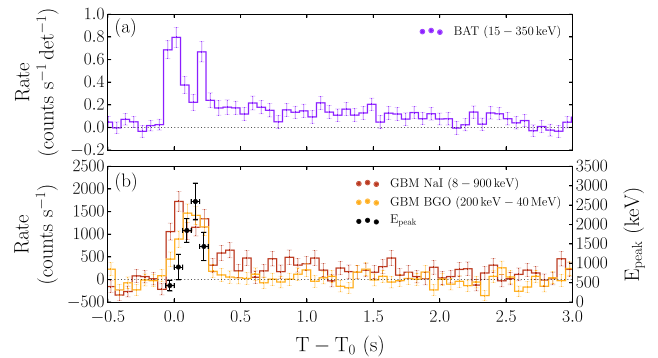


Figure 1. GRB 180618A light curves at 64 ms resolution as detected by the BAT and the GBM instruments. (a) Count rate per enabled detector of the 15–350 keV energy band of the BAT. (b) Count rates of the 8–900 keV energy band of the GBM sodium iodide (NaI) detector, and the 200 keV–40 MeV of the GBM bismuth germanate (BGO) detector. In a different y-axis, we present the evolution of the peak energy (E_{peak}); the values were derived from a cutoff power-law model fit to the 8 keV–40 MeV νF_ν spectrum. In the x-axis, T_0 corresponds to the BAT trigger time.

Unless stated otherwise, all uncertainties reported in this paper are given at the 1σ confidence level.

2. Observations and Data Reduction

On 2018 June 18 at $T_0 = 00:43:13$ universal time (UT), the BAT from the Neil Gehrels Swift Observatory triggered an alert for GRB 180618A (Meegan et al. 2009; LaPorte et al. 2018). GRB 180618A was detected by the BAT (Barthelmy et al. 2005; Sakamoto et al. 2018), the Gamma-ray Burst Monitor (GBM; Meegan et al. 2009; Hamburg et al. 2018), and the Konus instrument from the Wind satellite (Aptekar et al. 1995; Svinkin et al. 2018) as a short-duration and spectrally hard bright GRB with a long-duration weak emission tail at low gamma-ray energies (see Figure 1). Further GRB 180618A detections include the Astrosat Cadmium Zinc Telluride Imager (CZTI; Singh et al. 2014; Sharma et al. 2018) and the Insight Hard X-ray Modulation Telescope (HXMT; Liu et al. 2020; Song et al. 2022).

2.1. Ultraviolet and Optical Light Curves

At 86 s after the detection of GRB 180618A by the BAT, the UVOT (Roming et al. 2005) from the Neil Gehrels Swift Observatory started optical observations in an unfiltered band (*white*). Subsequently, the UVOT continued observations with the *uvw1*, *uvw2*, *uvw2* ultraviolet and the *v*, *b*, *u* optical filters (see Figure 2). At 202.5 s after the BAT alert, the 2 m fully robotic LT (Steele 2004)—with site at Roque de Los Muchachos Observatory (ORM; Spain)—automatically started follow-up observations (Guidorzi et al. 2006) with the RINGO3 three-band polarimeter and imager (Arnold et al. 2012). The LT observations consisted of three consecutive observing sequences of 10 minutes each with RINGO3 in three simultaneous bands (*BV*, *R*, *I*), followed by six single 10 s exposures with the *r* filter of the IO:O optical wide-field camera¹⁵ and two extra observation sets of 10 minutes with RINGO3. Three 300 s exposures with the IO:O *g*, *r*, *i* filters were also scheduled via the LT *phase2UI*¹⁶ and autonomously executed by the LT 7.4×10^4 s post-burst.

¹⁵ <https://telescope.livjm.ac.uk/TelInst/Inst/IOO/>

¹⁶ <https://telescope.livjm.ac.uk/PropInst/Phase2/>

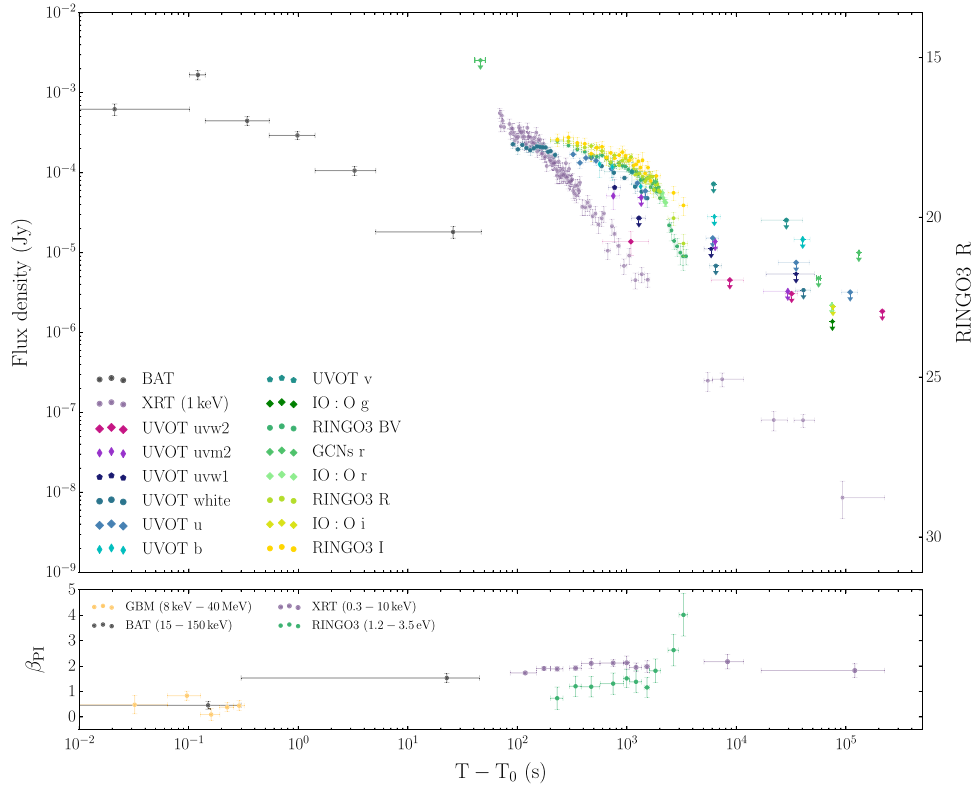


Figure 2. GRB 180618A light curves at the gamma-ray, X-ray, ultraviolet and optical bands. The data correspond to the Swift BAT, Swift XRT, Swift UVOT *white*, *v*, *b*, *u*, *uvw1*, *uvm2*, *uvw2* bands; LT RINGO3 *BV*, *R*, *I* bands; and LT IO:O *g*, *r*, *i* bands. The Swift BAT and XRT observations were obtained from the web interface provided by the Leicester University (Evans et al. 2009); the BAT data were binned to a signal-to-noise ratio of 7, and the absorbed 0.3–10 keV XRT light curve was converted to the observed flux density at 1 keV. For completeness, we include the optical observations and upper limits reported in the Gamma-ray Coordination Network (GCN) from the MASTER II (Tyurina et al. 2018), Tien Shan Astronomical Observatory (Mazaeva et al. 2018), and Xinglong-2.16 m (Zhu et al. 2018). Note that the GCN observations do not include filter corrections. In the *x*-axis, T_0 corresponds to the BAT trigger time. In the *y*-axis, the flux density is converted to the RINGO3 *R* magnitude. Detections have 1σ error bars, and nondetections are presented as 3σ upper limits—note that the MASTER data have 5σ upper limits. In the bottom panel, we present the temporal evolution of the photon index in the GBM 8 keV–40 MeV gamma-ray band, the BAT 15–150 keV gamma-ray band, the XRT 0.3–10 keV X-ray band, and the RINGO3 1.2–3.5 eV optical band.

The UVOT photometry (Vega; see Table 1) was derived from Level 1/2 products, which are already preprocessed by the telescope pipeline. We used the Level 1 event products to get a higher temporal resolution. They were converted into sky-coordinated data with the *coordinator* tool from the *HEASoft* v6.22.1 package (Blackburn 1995), and the hot pixels were removed with *uvotscreen*. The photometry was background-subtracted and measured with *uvotevtlc* using the default aperture radius of $5''$ from the instrument calibration (Poole et al. 2008; Breeveld et al. 2011). For the Level 2 images, we used the equivalent *uvotsource* tool. Furthermore, the images were aligned with *uvotskycorr* and co-added with *uvotisum*, requiring a minimum significance of 3σ for the detection of the optical transient. The stacked frames in which the optical transient did not reach the signal-to-noise ratio threshold are reported as 3σ flux upper limits in Table 1.

RINGO3 photometry (Vega; see Table 1) was derived by integrating the source photon counts across the eight polaroid positions (e.g., Jordana-Mitjans et al. 2020)—thus canceling any polarization signal. Each 10 minutes of integration consist of 10 single 1 minute exposures (see Figure 3), from which we individually derived the photometry using the *Astropy Photutils* package (Bradley et al. 2016). If the signal-to-noise ratio did not reach a minimum 3σ significance, we co-added consecutive frames. The RINGO3 magnitudes and flux density were absolute-calibrated in the Vega system following a standard procedure (see, e.g., Jordana-Mitjans et al. 2020) with

Table 1
GRB 180618A Ultraviolet and Optical Photometry Corresponding to the Swift UVOT *white*, *v*, *b*, *u*, *uvw1*, *uvm2*, *uvw2* Bands; LT RINGO3 *BV*, *R*, *I* Bands; and LT IO:O *g*, *r*, *i* Bands

Band	$t_{\text{mid}} - T_0$ (s)	$t_{\text{exp}}/2$ (s)	mag	mag _{err}	F_ν (Jy)	$F_{\nu, \text{err}}$ (Jy)
<i>white</i>	91	5	17.32	0.13	2.27e-04	2.7e-05
<i>white</i>	101	5	17.48	0.14	1.96e-04	2.6e-05
<i>white</i>	111	5	17.34	0.13	2.23e-04	2.6e-05
<i>white</i>	121	5	17.44	0.13	2.04e-04	2.5e-05
<i>white</i>	131	5	17.51	0.14	1.91e-04	2.5e-05
<i>white</i>	141	5	17.45	0.13	2.02e-04	2.5e-05
<i>white</i>	151	5	17.39	0.13	2.13e-04	2.5e-05
<i>white</i>	161	5	17.40	0.13	2.11e-04	2.5e-05
<i>white</i>

Note. t_{mid} corresponds to the mean observing time, T_0 is the BAT trigger time, and t_{exp} is the length of the observing time window. Note that the photometry is not corrected for neither Galactic, i.e., with reddening $E(B - V)_{\text{MW}} = 0.065 \pm 0.003$ (Schlegel et al. 1998), nor host galaxy extinction. Table 1 is published in its entirety in machine-readable format. A portion is shown here for guidance regarding its form and content.

(This table is available in its entirety in machine-readable form.)

observations of five dereddened A0-type stars (BD +30 2355, BD +67 675, BD +25 2478, HD 96781, HD 208368; Høg et al. 2000). The standard stars and the GRB 180618A

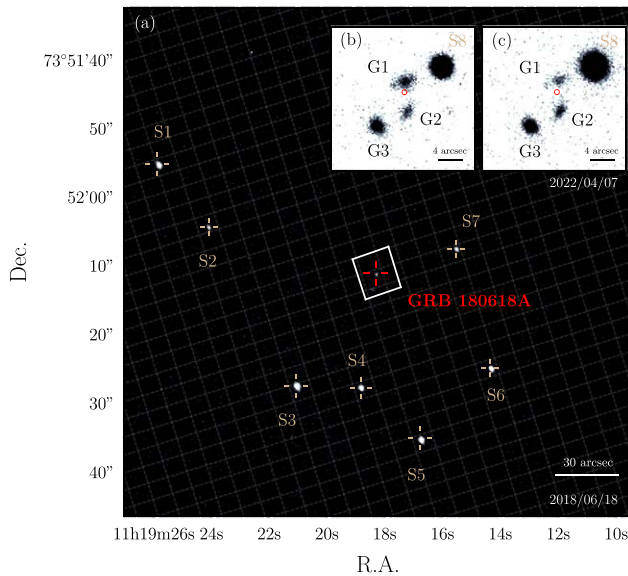


Figure 3. Observing fields of the GRB 180618A sky region. The GRB 180618A location is labeled in red, the stars (S) in light brown, and the galaxies (G) in black. (a) The 2 m LT *I*-band RINGO3 image of the GRB 180618A optical transient. (b) The *r*-band LBC image from the 8.4 m LBT. (c) The LBT *z*-band image. The field of view of the magnified LBT images corresponds to the white rectangle of panel (a). The LBT images reveal three galaxies at a similar redshift near the UVOT subarcsec localization of GRB 180618A (shown in red at the 90% confidence level). The G1 is the host galaxy of short GRB 180618A, with spectroscopic redshift $z = 0.554 \pm 0.001$.

field observations were scheduled via the LT *phase2UI* using the same instrumental setup of the night of the burst, and they were executed on 2019 June 13 and 16. This spectral calibration added a ≈ 0.07 mag uncertainty to the photometry. To test the instrument stability during observations, we checked the flux variability of five stars in the GRB 180618A field of view (see Figure 4). Using the temporal binning of the GRB 180618A light curves, the stars displayed on average a ≈ 0.04 mag deviation from the mean.

The IO:O camera photometry (AB; see Table 1) was derived for each of the 10 s individual frames. For the observing sequence 7.4×10^4 s post-burst, we integrated the observations into a single 900 s exposure per band. The optical transient was not detected, and the flux upper limits are presented in Table 1 at the 3σ confidence level. We calibrated the IO:O bands by crossmatching 10 12–17 mag stars from the Sloan Digital Sky Survey (SDSS) Data Release 12 catalog (Alam et al. 2015).

2.2. Optical Polarimetry

In the RINGO3 configuration, we measure the polarization of a source by extracting the flux at each of the eight polaroid positions (e.g., Jordana-Mitjans et al. 2020), which we then convert to Stokes parameters ($q-u$) following Clarke & Neumayer (2002). The polarization uncertainties are derived from a Monte Carlo error propagation, starting from 10^6 flux values.

We measured the instrumental $q-u$ using ≈ 75 measurements of seven unpolarized standards per band (BD +32 3739, BD +33 2642, BD +28 4211, HD 212311, HD 14069, HD 109055, G191B2B; Turnshek et al. 1990; Schmidt et al. 1992), which were observed during 200 days before and 10 days after the date of the burst. Note that we used an asymmetric time window of data given a small shift of $\Delta u \approx 0.005$ in the

instrumental u parameter 10 days post-burst. For the chosen time window, there was no significant drift of the instrumental $q-u$, and the Pearson’s correlation coefficients were low $|r| < 0.1$ with p -values > 0.3 .

To derive the most constraining polarization measurement for GRB 180618A, we used the entire 10 minutes epoch corresponding to $t_1 = 203$ –800 s post-burst of the *BV* band, which is the RINGO3 band with the highest signal-to-noise ratio. We detected the optical transient at a signal-to-noise ratio of ≈ 27 in each of the eight images of the polaroid. At this signal-to-noise ratio level, the observed polarization ($P \approx 1\%$) was within the instrument sensitivity, and we estimate a 2σ upper limit of $P_{BV} < 6.1\%$. Due to the slowly fading emission during the second and third observing epochs, $t_2 = 822$ –1417 s and $t_3 = 1438$ –2035 s post-burst, respectively, the polarization upper limits could still be derived but were less well constrained, with $P_{BV, \{t_2, t_3\}} < 10.7\%$, 17.0% (2σ). For the *R* and *I* bands, the 2σ upper limits for the three epochs are $P_{R, \{t_1, t_2, t_3\}} < 14.5\%$, 30.2% , 37.0% and $P_{I, \{t_1, t_2, t_3\}} < 23.5\%$, 36.8% , 38.6% . We note that the RINGO3 depolarization factor (Jordana-Mitjans et al. 2021) is negligible in the *BV* band ($D_{BV} = 1$) and small in the *R* and *I* bands ($D_{\{R, I\}} = 0.98, 0.94$).

2.3. LBT Photometry

To search for the GRB 180618A host galaxy, and thus determine the GRB 180618A redshift, we used the LBT (Hill et al. 2006)—an optical/infrared telescope with twin 8.4 m mirrors located on the Mt. Graham International Observatory, Arizona, USA.

On 5 April 2022, deep-field *r*- and *z*-band imaging of the GRB 180618A location were acquired with the LBC (Ragazzoni et al. 2000; Giallongo et al. 2008). The total exposure time for each filter was 36 minutes, and the data were reduced with the data reduction pipeline developed by the Istituto Nazionale di Astrofisica (INAF-Osservatorio Astronomico di Roma; Fontana et al. 2014), which includes bias subtraction and flat-fielding, bad-pixel and cosmic-ray masking, astrometric calibration, and co-addition. The average seeing was $\approx 1''.4$, and the mean airmass of the observations was ≈ 1.4 . The LBC photometry (AB) achieved limiting magnitudes of $r_{\text{lim}} = 26.3$ mag and $z_{\text{lim}} = 25.6$ mag (3σ limits). In both images, we found three galaxies (G1, G2, and G3; see Figure 3) at a projected angular distance of $d_{G1} = 1''.6$, $d_{G2} = 3''.7$, and $d_{G3} = 7''.7$ from the UVOT subarcsec localization of GRB 180618A (Siegel et al. 2018). The G3 galaxy was already cataloged by the SDSS (Alam et al. 2015), with a photometric redshift of $z_{G3} = 0.54 \pm 0.03$, and brightness $r_{\text{band}, G3} = 22.4 \pm 0.3$ mag and $z_{\text{band}, G3} = 21.2 \pm 0.6$ mag. The G1 and G2 galaxies were uncatalogued in the SDSS but identified in the O’Connor et al. (2022) and Fong et al. (2022) surveys of short GRBs host galaxies. From the LBC images, we measured $r_{\text{band}, G1} = 22.98 \pm 0.06$ mag, $r_{\text{band}, G2} = 23.58 \pm 0.11$ mag in the *r* band, and $z_{\text{band}, G1} = 22.62 \pm 0.10$ mag, $z_{\text{band}, G2} = 22.48 \pm 0.09$ mag in the *z* band.

2.4. LBT Spectroscopy

On 2022 April 8, optical spectroscopy of the G1 and G2 galaxies was obtained with the MODS (Pogge et al. 2010), i.e., MODS-1 and MODS-2. Each MODS contains a red and blue channel for spectroscopy. Both MODS were configured to use the dual grating mode ($0.32 \mu\text{m}$ – $1.05 \mu\text{m}$ coverage) and a $1''.2$ wide slit ($R \approx 630$ – 1350 resolution). A position angle of 179.3°

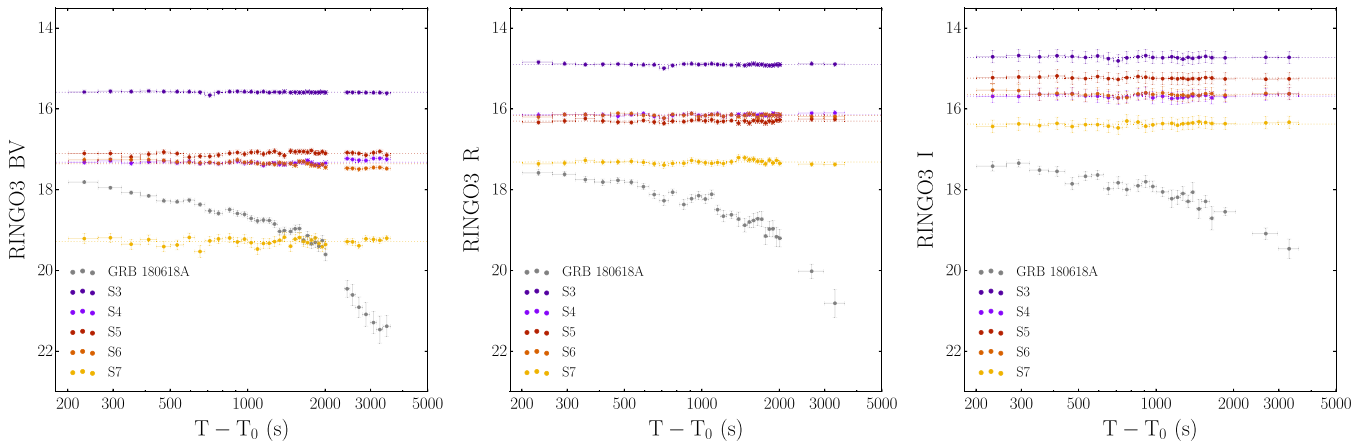


Figure 4. RINGO3 photometric analysis of the field stars (S) in Figure 3 using the temporal binning of the GRB 180618A light curves. Note that stars S1 and S2 are not included in the analysis because the LT repointed to the GRB 180618A coordinates after the IO:O observations, and they fall outside of the revised RINGO3 field of view. From left to right, panels correspond to the RINGO3 *BV*, *R*, and *I* bands.

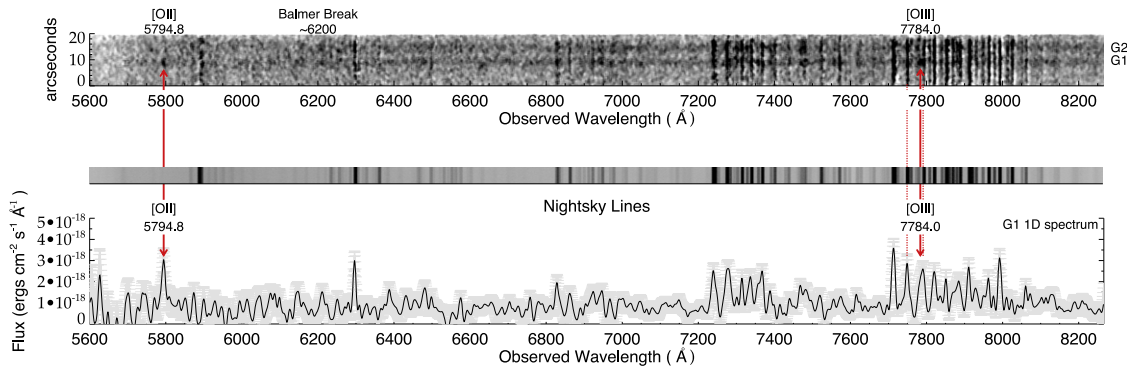


Figure 5. From top to bottom: two-dimensional MODS-2 spectra of the galaxy G2 and the GRB 180618A host galaxy (G1), corresponding night-sky emission lines, and one-dimensional spectrum of the G1 galaxy. In the G1 spectrum, we identify two oxygen emission lines (corresponding to [O II] and [O III]) redshifted at $z = 0.554 \pm 0.001$. The night-sky spectrum displayed here demonstrates that both oxygen emission lines (marked in solid red arrows) are not unsubtracted night-sky emission lines; the [O II] line is not coincident with any night-sky line, and the [O III] line is found between two (dotted red lines).

was used for observations. The position angle was selected so that the target galaxies and the foreground star ($\approx 47''$ away) were vertically aligned. The foreground star was aligned in the center of the slit as the target galaxies were too faint to be detected in the acquisition images without incurring too large of an overhead. Two exposures of 20 minutes each were obtained in each channel, with each MODS. The mean airmass of the observations was ≈ 1.85 . The mean seeing (as measured from the off-axis wave front sensor and guiders) was $1.92 \pm 0''.05$ and $1.84 \pm 0''.04$ for MODS-1 and MODS-2, respectively. Observations of the spectrophotometric star BD +33 2642 were used to flux calibrate the data and remove the instrumental signatures from the data.

The MODS data were reduced first with the *modsCCDRed* v2.04 package developed by the MODS team (Pogge 2019) to remove the bias and flat-field the data using a slitless pixel flat. Next, custom IRAF scripts (Tody 1986) were used to extract along the central slit using a stellar trace. The observations of the spectrophotometric standard were combined to measure the trace of the dispersion along the entire slit. This trace was used along with the wavelength calibration from arc-lamp lines to rectify the tilt in both x and y directions for the full frame (8192 pixels \times 3072 pixels). This step made the x -axis parallel to the dispersion direction and the y -axis purely parallel with the

spatial extent along the slit. Final wavelength calibration was cross-checked with known strong auroral skylines in the blue ([O I] $\lambda = 5577.3$ Å) and red ([O I] $\lambda = 6300.3$ Å) channels. One-dimensional spectra were then extracted from each channel using a $1''.85$ wide aperture. This value was chosen to match the mean seeing of the observations, maximizing the signal-to-noise ratio. Next, the spectra were flux-calibrated using the spectrophotometric standard star. Telluric features were removed from the red channels using a normalized spectrophotometric standard spectrum.

Inspection of the data showed no flux from the galaxies in the blue channels of both MODS. A faint but significant continuum was detected for the galaxies in MODS-2 (see Figure 5), but not in MODS-1. The absence of flux in MODS-1 is consistent with a known technical issue¹⁷ in which the sensitivity of the instrument has decreased by a factor of 1.6 since the 2011 commissioning. As a sanity check, the acquisition images were rechecked to confirm no differences in the alignment of the foreground star. The continua of the target galaxies are clearly visible in the individual background-subtracted exposures for the red channel of MODS-2 (see Figure 5). The spatial position (y direction) of the continua

¹⁷ <https://scienceops.lbto.org/mods/preparing-to-observe/sensitivity/>

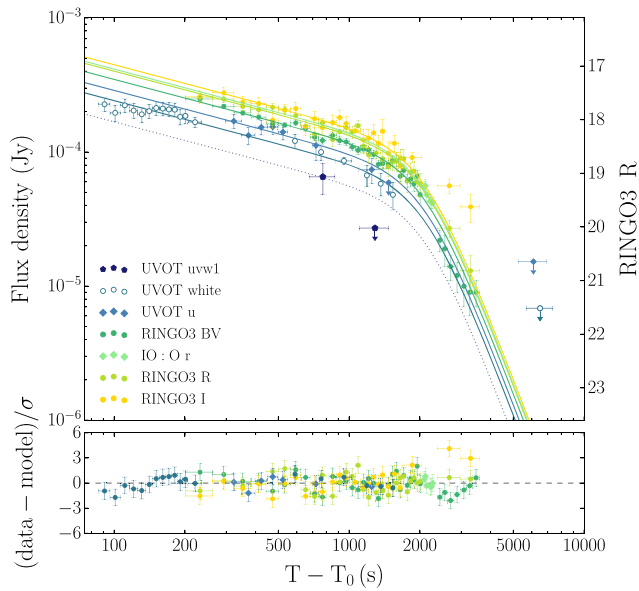


Figure 6. RINGO3 *BV*-, *R*-, *I*-band and UVOT *white*-, *u*-band data modeled with smoothly connected broken power laws that have a common time break across bands. The results of the fit are a break at $t_{\text{break}} = 2120 \pm 60$ s post-burst and power-law indexes of $\alpha_1 = 0.46 \pm 0.02$ pre-break and $\alpha_2 = 4.6 \pm 0.3$ post-break with $\chi^2/\text{dof} = 128/116$. We also show with a dotted line the best-fitting model normalized to the near-ultraviolet UVOT *uvw1* band, which has a power-law decay $\alpha_{\text{uvw1}} > 1.7$ pre-break. Detections have 1σ error bars, and nondetections are presented as 3σ upper limits.

from the target galaxies detected in the MODS-2 red channel exactly matched the angular separation between them and the foreground alignment star—as measured from the LBC images (see Figure 3). The final calibrated MODS-2 red channel data have a fixed instrumental resolution of 8.19 \AA per resolution element covering $5600\text{--}10100 \text{ \AA}$, which corresponds to a resolution of $R \approx 630\text{--}1350$ and $0.84 \text{ \AA pixel}^{-1}$. These values were confirmed using the arc lamps.

3. Results

In Section 3.1, we present the temporal and spectral analysis of the optical emission. In Section 3.2, we estimate the redshift of GRB 180618A using the ultraviolet and optical photometry of the transient emission, and we then associate GRB 180618A with its host galaxy. In Sections 3.3–3.5, we study the gamma-ray properties of short GRB 180618A and its extended gamma-ray emission.

3.1. Optical Emission

We simultaneously fitted the UVOT *white*, RINGO3 *BV*, *R*, *I*, and IO:O *r* optical light curves with smoothly connected broken power laws (Beuermann et al. 1999; Molinari et al. 2007), i.e., $F = F_0[(t/t_{\text{break}})^{\alpha_1} + (t/t_{\text{break}})^{\alpha_2}]^{-1/n}$, fixing the time break across bands and the smoothness parameter to $n = 1$ for convergence (Piranomonte et al. 2008). This serves to help us understand the overall decay rate of the emission, as well as to check for color evolution in the residuals of the best-fitting model. The emission initially decays with $\alpha_{\text{opt},1} = 0.46 \pm 0.02$ and suffers a sharp break at $t_{\text{break}} = 2120 \pm 60$ s post-burst, with $\alpha_{\text{opt},2} = 4.6 \pm 0.3$ (see Figure 6).

This extreme flat-to-steep decay evolution is rare in GRB light curves. To our knowledge, the only other GRB that has shown a similar flat-to-steep decay rate transition

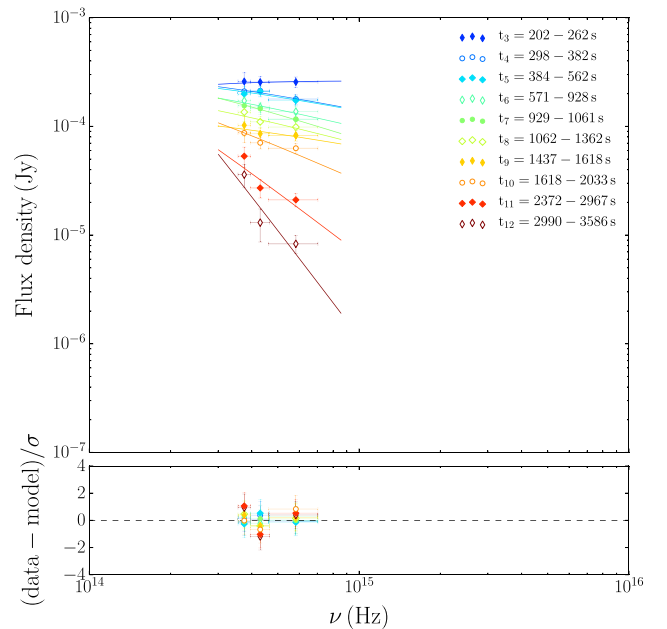


Figure 7. Modeling of the GRB 180618A RINGO3 optical emission with power-law models. Note that the model accounts for Galactic dust extinction but does not include the host galaxy dust contribution.

($\alpha_{\text{opt},1} = 0.44_{-0.21}^{+0.08}$ to $\alpha_{\text{opt},2} = 5.3 \pm 0.2$) was found in the fainter optical emission of short GRB 070707 (Piranomonte et al. 2008) and at a much later time, ≈ 1.8 days post-burst. In addition, in GRB 180618A the spectral evolution across the break is chromatic; the RINGO3 *I*-band emission is significantly underestimated by $>3\sigma$ after the break, and the normalized best-fitting model overestimates the 3σ photometric upper limit of the near-ultraviolet UVOT *uvw1* band. Furthermore, we individually fitted the flux decay rate of the RINGO3 *BV*, *R*, *I* and IO:O *r* bands after the break with a power law, finding moderate slopes for redder bands, i.e., $\alpha_{\text{opt},\{BV,R,I\}} = 4.6 \pm 0.5, 3.5 \pm 0.5, 3.2 \pm 0.1, 1.4 \pm 0.2$.

Using Xspec v12.9.1 (Arnaud 1996) and χ^2 statistics, we modeled the RINGO3 data with a power law that accounts for Milky Way dust extinction, i.e., $E(B - V)_{\text{MW}} = 0.065 \pm 0.003$ (Schlegel et al. 1998). We find that the optical photon index significantly evolves during observations, from $\beta_{\text{opt,PI}} = 0.7 \pm 0.4$ at $t = 202\text{--}263$ s post-burst to $\beta_{\text{opt,PI}} = 4.0 \pm 0.8$ at $t = 2990\text{--}3586$ s post-burst; see results in Figure 2 (bottom panel), Figure 7, and Table 2. Note that if we include the UVOT data, we need to add the host galaxy dust extinction to the model, which shifts all optical photon indexes by the same amount toward harder values (i.e., the relative evolution of the $\beta_{\text{opt,PI}}$ remains the same).

3.2. Redshift and Host Galaxy

We rule out a high-redshift origin given the detection of the GRB 180618A optical counterpart with all the UVOT filters (Krühler et al. 2011). We used the *uvot2pha* tool to convert the UVOT data to Xspec spectral files, and a dust-absorbed power law that includes both Milky Way and host galaxy contributions, i.e., $E(B - V)_{\text{HG}}$. Taking the spectral coverage up to the far-ultraviolet of the UVOT *uvw2* filter into account and using the redshifted Lyman-limit break at $\lambda_{\text{obs}} = 912(1 + z) \text{ \AA}$, we fitted the co-temporal UVOT and RINGO3 data corresponding to $550\text{--}1600$ s post-burst using χ^2 statistics. We estimate a

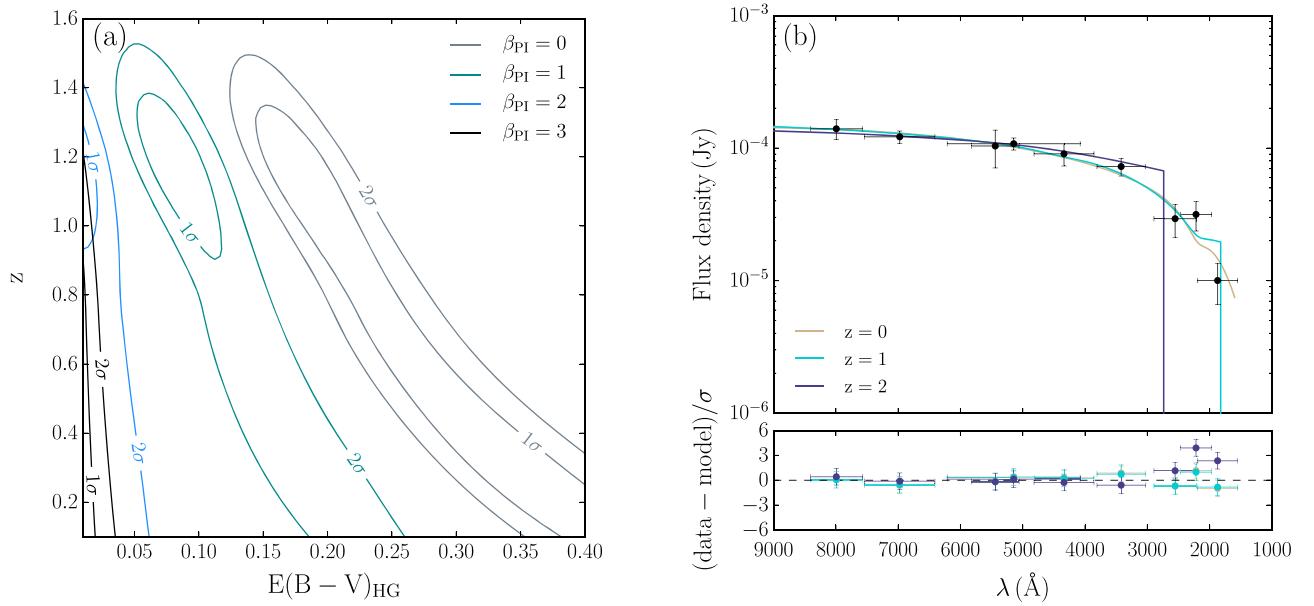


Figure 8. Estimation of the GRB 180618A redshift from the co-temporal GRB 180618A UVOT and RINGO3 data modeled with a dust-absorbed power law that includes the redshifted Lyman-limit break. (a) χ^2 distribution of the best-fitting redshifts for different values of the host galaxy extinction $E(B-V)_{\text{HG}}$ and photon index β_{PI} . The confidence level contours at the 2σ level indicate a redshift $z < 1.5$ for GRB 180618A. (b) Best-fitting models for redshifts $z = 0, 1, 2$.

Table 2

GRB 180618A Optical Photon Indexes ($\beta_{\text{opt,PI}}$) Derived from the Best-fitting Power-law Models to the RINGO3 Data

$t_{\text{mid}} - T_0$ (s)	t_{err} (s)	$\beta_{\text{opt,PI}}$	$\beta_{\text{opt,PI, err}}$
231	30	0.7	0.4
340	42	1.2	0.4
473	89	1.2	0.4
749	179	1.3	0.4
995	67	1.5	0.4
1212	150	1.4	0.4
1528	90	1.2	0.4
1825	208	1.8	0.5
2670	298	2.6	0.6
3288	298	4.0	0.8

Note. t_{mid} is the mean observing time, T_0 is the BAT trigger time, and t_{err} is half the length of the observing time window. Note that the model does not account for host galaxy extinction.

redshift $z < 1.5$ at the 2σ confidence level from the $E(B-V)_{\text{HG}} - \beta_{\text{PI}} - z$ parameter space (see Figure 8(a)). Note that not knowing the GRB 180618A intrinsic spectral slope does not affect the redshift constraint but adds large uncertainty in determining the host galaxy dust contribution. See also the best-fitting models for redshifts $z = 0, 1, 2$ in Figure 8(b).

Among all three candidate galaxies detected in the LBT images, G1 is the most likely host galaxy of GRB 180618A given its proximity (see Figure 3). In the G1 galaxy spectrum (see Figure 5), we detect two emission lines at $\lambda_{\text{obs, O II}} = 5794.8 \text{ \AA}$ and $\lambda_{\text{obs, O III}} = 7784.0 \text{ \AA}$, corresponding to the unresolved [O II] $\lambda = 3726\text{--}3729 \text{ \AA}$ doublet and the [O III] $\lambda = 5007 \text{ \AA}$ line, respectively. This implies a spectroscopic redshift of $z_{\text{G1}} = 0.554 \pm 0.001$ for the G1 galaxy. This value is consistent with O’Connor et al. (2022) and Nugent et al. (2022) estimates of photometric redshifts of $z = 0.4^{+0.2}_{-0.1}$ and $z = 0.52^{+0.09}_{-0.11}$, respectively. We find that the probability of an accidental alignment (Bloom et al. 2002; Berger 2010;

Fong & Berger 2013) of GRB 180618A and the G1 galaxy is low, with $p_d \approx 0.02$. Therefore, we associate the G1 redshift ($z = 0.554$) with GRB 180618A. For the G2 galaxy spectrum, we do not detect emission lines. However, there is a clear drop of the continuum flux blueward of $\lambda_{\text{obs}} \approx 6200 \text{ \AA}$ that we identify as the $\lambda = 4000 \text{ \AA}$ break, corresponding to a redshift of $z_{\text{G2}} \approx 0.55$. Therefore, the LBT spectroscopic analysis suggests that all three galaxies (G1, G2, and G3) are at a similar redshift.

GRB 180618A lies in the outskirts of its host, 10 kpc from the center of the galaxy (see also O’Connor et al. 2022; Fong et al. 2022). This is consistent with the large offsets found in short GRBs and in disagreement with those of long GRBs (Berger 2010; Fong & Berger 2013; Behroozi et al. 2014; Fong et al. 2022). Note that short GRBs are usually found with offsets to star-forming disk galaxies or even further away from their elliptical host (Fong & Berger 2013; Behroozi et al. 2014). Similar to the environment of GRB 180618A, Fong & Berger (2013) found that about 30%–45% of short GRBs happen where there is no optical light, i.e., negligible stellar mass. Like GRB 180618A, most short GRBs display signs of migration from their birth sites, likely due to natal kicks in binaries (Rosswog et al. 2003; Kelley et al. 2010; Fong & Berger 2013). This is consistent with short GRBs exploding in low ambient density, thus producing fainter afterglows (Berger 2010; Kann et al. 2011; Fong et al. 2015).

3.3. Duration of the Prompt Gamma-Ray Emission

We calculated the duration (T_{90}) of GRB 180618A (Lien et al. 2016; Moss et al. 2022), corresponding to the time interval in which 90% of the burst fluence is released, using the 64 ms binned and background-subtracted GRB 180618A light curves of the BAT. Using the *battblocks* tool (Scargle 1998), a *FTOOLS* released as part of *HEASoft* (Blackburn 1995), we find $T_{90} = 45 \pm 10$ s for the low-energy spectral range of the BAT (i.e., 15–100 keV), and $T_{90} = 0.26 \pm 0.14$ s at 100–350 keV. The duration of GRB 180618A at the low-

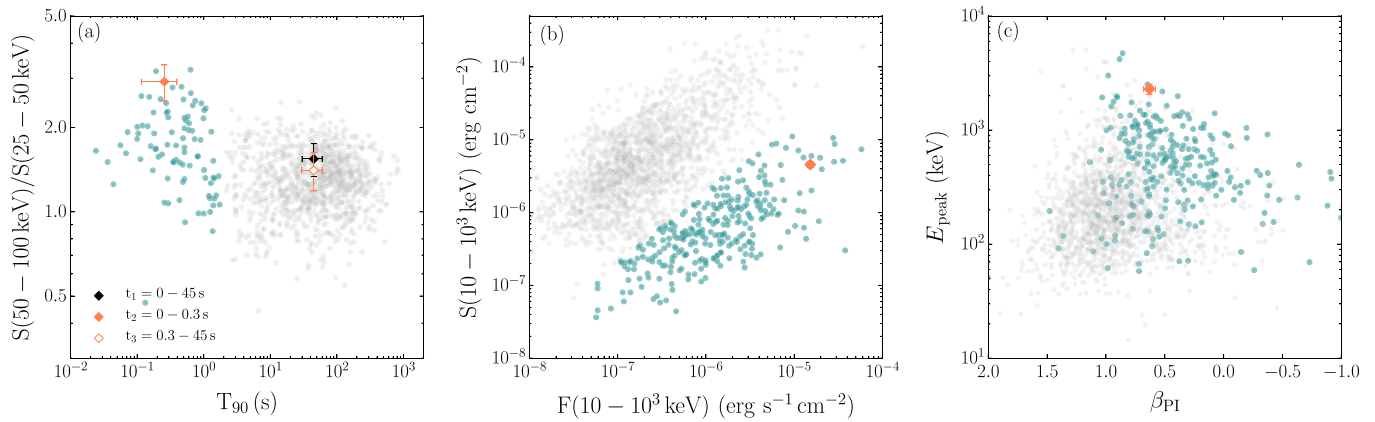


Figure 9. High-energy properties of GRB 180618A and comparison with catalog GRBs; those with duration $T_{90} > 2$ s are displayed in gray, and those with $T_{90} < 2$ s in blue (Kouveliotou et al. 1993). (a) BAT-band hardness ratio and duration of GRB 180618A (t_1), the ≈ 0.3 s short gamma-ray pulse (t_2), and its ≈ 45 s extended gamma-ray emission (t_3). The background data correspond to the short hard and long soft bimodal clustering of the BAT GRB catalog (Kouveliotou et al. 1993; Lien et al. 2016). (b) Comparison of the ≈ 0.3 s short GRB 180618A flux F and the fluence S (marked in orange) with the GRB sample from the GBM catalog (von Kienlin et al. 2020; Poolakkil et al. 2021). Note that the GRB 180618A flux and fluence have been recalculated to match the $10\text{--}10^3$ keV energy range of the GBM catalog. (c) Photon index β_{PI} and peak energy E_{peak} of GRB 180618A (marked in orange).

energy bands is 2 orders of magnitude higher than at high-energy bands, confirming two spectral components: a short hard GRB and extended soft gamma-ray emission below the 100 keV energy band (Hamburg et al. 2018; Sakamoto et al. 2018; Svinkin et al. 2018). We find that the 0.3 s short-duration GRB 180618A belongs to the hardness–duration cluster of short GRBs, and that it is one of the hardest to have been detected by the BAT (within the top $\approx 0.5\%$; see Figure 9-a). Note also that Sakamoto et al. (2018) found negligible spectral lag for the short-duration gamma-ray pulse of GRB 180618A—a spectral property typical of short hard GRBs.

Furthermore, GRB 180618A is a classically short GRB in terms of the duration reported in the GBM GRB catalog (von Kienlin et al. 2020), with $T_{90}(50\text{--}300\text{ keV}) = 3.7 \pm 0.6$ s. For the GBM, von Kienlin et al. (2020) found that the threshold separating short and long GRBs is $T_{90} = 4.2$ s—instead of the $T_{90} \approx 2$ s of the Burst And Transient Source Experiment (BATSE; Kouveliotou et al. 1993).

3.4. Spectral Properties of the Prompt Gamma-Ray Emission

We performed a Swift BAT and Fermi GBM joint spectral fit in RMFit¹⁸ v4.3.2. We used the GBM time-tagged events (TTE) data from the NaI 3/4 and BGO 0/1 detectors, from which we selected the 8–900 keV and 200 keV–40 MeV spectral regimes, respectively. The 15–150 keV BAT spectra were extracted with the *batbinevt* tool. Using C-statistics, we modeled the νF_ν spectrum of the ≈ 0.3 s short GRB with a simple power law. A power-law model overestimates the data over ≈ 1 MeV; consequently, we modeled the high-energy break with a cutoff power-law model (see, e.g., Poolakkil et al. 2021). The best-fitting model suggests that the νF_ν spectrum has a hard slope with mean photon index $\beta_{\text{PI}} = -\alpha_{\text{CL}} = 0.63 \pm 0.05$, peak energy $E_{\text{peak}} = 2290 \pm 238$ keV, and fluence $S(10\text{--}10^4\text{ keV}) = (5.6 \pm 0.4) \times 10^{-6}$ erg cm^{-2} . The photon index is average compared to other short hard GRBs detected by the GBM (von Kienlin et al. 2020; Poolakkil et al. 2021). Yet, GRB 180618A is one of the hardest and most energetic gamma-ray pulses among short GRBs; it is within the $\approx 1\%$ percentile in terms of the high-frequency peak energy and

within the top $\approx 5\%$ in terms of the total energy released (see Figures 9(b), (c)).

For the spectrum corresponding to the $\approx 0.3\text{--}45$ s extended gamma-ray emission, the best-fitting photon index of the power-law model is $\beta_{\text{PI}} = 1.51 \pm 0.09$. This intermediate photon index suggests that the spectrum has a cutoff (e.g., Poolakkil et al. 2021). In order to constrain the peak energy, we fixed the low-energy index of the cutoff power-law model to the average of the GBM catalog (Poolakkil et al. 2021) of short ($\alpha_{\text{CL}} = -0.6$) and long GRBs ($\alpha_{\text{CL}} = -1$). We find $E_{\text{peak}} = 87 \pm 18$ keV and $S(10\text{--}10^4\text{ keV}) = (6 \pm 1) \times 10^{-7}$ erg cm^{-2} for $\alpha_{\text{CL}} = -0.6$, and $E_{\text{peak}} = 125 \pm 45$ keV and $S(10\text{--}10^4\text{ keV}) = (8 \pm 2) \times 10^{-7}$ erg cm^{-2} for $\alpha_{\text{CL}} = -1$, consistent with the Svinkin et al. (2018) findings.

To determine the temporal evolution of the photon index and the peak energy, we fitted a cutoff power-law model to the 8 keV–40 MeV GBM spectrum of each light-curve bin. To avoid merging peaks and valleys, we used a constant binning as opposed to a fixed signal-to-noise ratio (e.g., Guiriec et al. 2010). Using the default 64 ms binned light curves, we find that in a time span of less than 260 ms, the peak energy increases from $E_{\text{peak}} = 427 \pm 138$ keV to $E_{\text{peak}} = 2593 \pm 473$ keV with constant photon index. As seen in other spectroscopically resolved short GRBs (Guiriec et al. 2010), the peak energy tracks the light curve with a strong soft–hard–soft spectral evolution in a short time period; see the peak energy evolution in Figure 1(b) and the photon index in Figure 2 (bottom panel).

3.5. Intrinsic Energetics

Short GRBs have typically lower fluences and thus follow a different peak energy (E_{peak}) and isotropic energy (E_{iso}) relation than long GRBs (Amati 2006; Ghirlanda et al. 2009). If we introduce the k-correction (Bloom et al. 2001) to the $1\text{--}10^4$ keV rest-frame energy band for redshift $z = 0.554$, we obtain an isotropic-equivalent energy $E_{\text{iso}} = (4.6 \pm 0.4) \times 10^{51}$ erg and luminosity $L_{\text{iso}} = (1.9 \pm 0.2) \times 10^{52}$ erg s^{-1} for short GRB 180618A, and $E_{\text{iso}} = (7 \pm 2) \times 10^{50}$ erg and $L_{\text{iso}} = (2.4 \pm 0.7) \times 10^{49}$ erg s^{-1} for the extended gamma-ray emission. See also the high-energy properties for redshifts $z = 0.01\text{--}1.5$ in Figure 10. For redshifts $z \gtrsim 0.1$, GRB 180618A lays within the cluster of short GRBs—it is one of the hardest

¹⁸ <https://fermi.gsfc.nasa.gov/ssc/data/analysis/rmfit/>

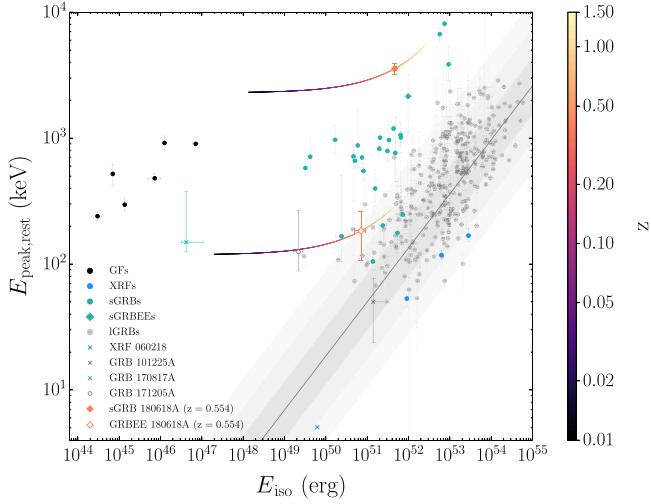


Figure 10. Rest-frame peak energy (E_{peak}) and isotropic-equivalent energy (E_{iso}) of short GRB 180618A and its extended gamma-ray emission at redshift $z = 0.554$. The GRB 180618A high-energy parameters are also displayed for the redshift range $z = 0.01$ – 1.5 . For reference, we include those GRBs with known redshifts classified as giant flares from magnetars (GFs; Zhang et al. 2020), short GRBs (sGRBs; D’Avanzo et al. 2014; Calderone et al. 2015; Tsvetkova et al. 2017, 2021), short GRBs with extended gamma-ray emission (sGRBEEs; D’Avanzo et al. 2014), long GRBs (IGRBs; Tsvetkova et al. 2017, 2021), and X-ray flashes (XRFs; Tsvetkova et al. 2021). For the population of long GRBs, we represent the best-fitting line from Tsvetkova et al. 2021, and the corresponding 1σ , 2σ , 3σ confidence levels. We also add the GRB counterpart of gravitational wave event GW170817 (Zhang et al. 2018), and three GRBs with early afterglows interpreted as blackbody emission from either a thermalized jet or cocoon: XRF 060218 (Campana et al. 2006; Thöne et al. 2011), GRB 101225A (Thöne et al. 2011), and GRB 171205A (D’Elia et al. 2018; Izzo et al. 2019).

and not compatible with the long GRB population. Overall, the gamma-ray properties and the GRB–host galaxy offset confirm the merger nature of GRB 180618A (see, e.g., Zhang et al. 2009; Rastinejad et al. 2022).

4. Interpretation and Modeling

The overall temporal and spectral evolution of the optical emission ($\Delta\alpha_{\text{opt}} = 4.2$, $\Delta\beta_{\text{opt}} = 3.3$; see Figure 2) are hard to explain just in terms of the flaring activity (i.e., $\Delta t/t > 1$; Zhang et al. 2006) or the external shock from the decelerating relativistic ejecta (i.e., the afterglow; Piran 1999; Kobayashi 2000). The observed decay rates of the emission do not agree with $\alpha \approx 1$ expected from forward shock emission with a typical electron index of the synchrotron energy spectrum, and the break cannot be reconciled with the passage of the synchrotron cooling frequency (Sari et al. 1998). We also discard the fast-fading emission from the reverse shock (Kobayashi 2000), which typically decays with index $\alpha \approx 2$ —still slower than in GRB 180618A. A reverse-shock scenario further disagrees with the rapid spectral evolution of the optical emission at the time of the light-curve break, and the nondetection of high values of polarization during the broad optical peak (Mundell et al. 2013). Finally, we rule out that the optical break is an effect of the relativistic collimation of the outflow given that there is no simultaneous steepening of the emission across the spectrum at that time (Sari 1999; Racusin et al. 2009).

We suggest that the spectral evolution and rapid decline in the optical emission of GRB 180618A is produced by thermal emission (e.g., Thöne et al. 2011; Izzo et al. 2019). In

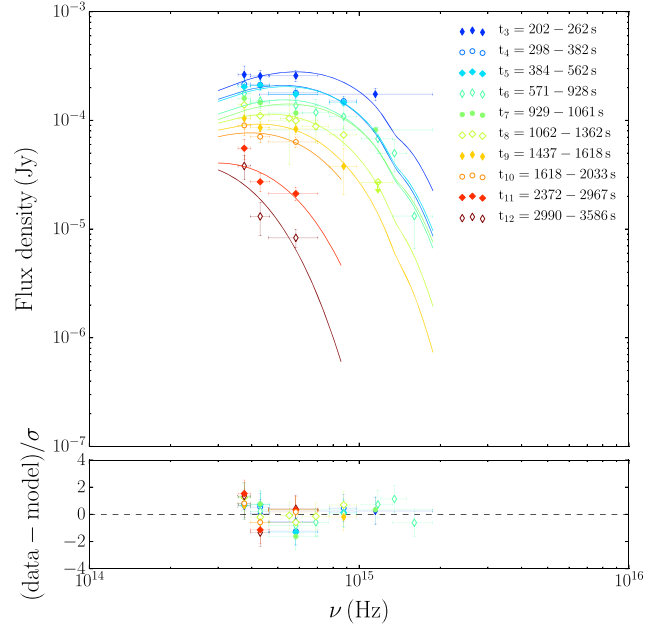


Figure 11. GRB 180618A best-fitting blackbody models to joint RINGO3/UVOT data at the observer rest frame. Note that the model accounts for Galactic dust extinction but does not include the host galaxy dust contribution.

Section 4.1, we model the ultraviolet to optical emission with a blackbody model. Following, we discuss if the radioactive decay of the r -processed ejecta from the merger or a thermalized jet are credible interpretations to explain the origin of the bright thermal emission. In Section 4.2, we find evidence of a magnetar wind nebula powering thermal optical emission for 15–60 minutes after GRB 180618A—suggesting that emission before that time is due to the jet afterglow. In Section 4.3, we detail the properties of the magnetar powering the distinct nonthermal emission components, from gamma rays to optical wavelengths. In Section 4.4, we model the overall (X-ray to optical) spectra with physical synchrotron models. This analysis proves Section 4.2 findings; the emission until 3–15 minutes post-burst is due to the jet afterglow and that corresponding to 15–60 minutes post-burst requires an extra spectral component (i.e., thermal emission). In Section 4.5, we test closure relations, and we suggest that the jet geometry and observer viewing angle are key to detecting the thermal emission.

4.1. Thermal Emission

In Xspec, we modeled the co-temporal UVOT and RINGO3 data with a blackbody profile that includes Milky Way dust absorption (see Figure 11). At the observer rest frame, the best-fitting effective temperatures and luminosities from the blackbody models evolve from $T_{\text{eff}} = (1.1 \pm 0.1) \times 10^4$ K and $L_{\text{th}}/D_L^2 = (4.3 \pm 0.5) \times 10^{44}$ erg s $^{-1}$ Gpc $^{-2}$ at $t = 202$ – 262 s post-burst to $T_{\text{eff}} = (3.8 \pm 0.6) \times 10^3$ K and $L_{\text{th}}/D_L^2 = (1.8 \pm 0.6) \times 10^{43}$ erg s $^{-1}$ Gpc $^{-2}$ at $t = 2990$ – 3586 s post-burst (see results in Table 3), where D_L is the luminosity distance. Note that the data are well fitted by the model without the need of the host galaxy dust extinction component, which is consistent with the large offset of short GRB 180618A with the host galaxy core (i.e., ≈ 10 kpc).

Faint thermal emission at optical and infrared wavelengths has been detected emerging hours to days after short GRBs

Table 3

GRB 180618A Effective Temperatures (T_{eff}) and Luminosities (L_{th}/D_L^2)
Derived from the Best-fitting Blackbody Models to Joint RINGO3/
UVOT Data

$t_{\text{mid}}-T_0$	t_{err}	T_{eff}	$T_{\text{eff, err}}$	L_{th}/D_L^2	$L_{\text{th, err}}/D_L^2$
(s)	(s)	(10^3 K)	(10^3 K)	(10^{43} erg s^{-1} Gpc $^{-2}$)	(10^{43} erg s^{-1} Gpc $^{-2}$)
231	30	10.9	1.0	42.6	5.3
340	42	9.8	0.7	27.9	2.2
473	89	10.0	0.5	27.9	0.7
749	179	9.8	0.6	20.7	1.7
995	67	10.2	0.6	19.8	1.0
1212	150	8.6	0.9	13.0	1.5
1528	90	7.8	1.1	9.4	1.2
1825	208	7.2	1.2	7.1	0.9
2670	298	5.3	0.9	2.6	0.3
3288	298	3.8	0.6	1.8	0.6

Note. t_{mid} is the mean observing time, T_0 is the BAT trigger time, t_{err} is half the length of the observing time window, and D_L is the luminosity distance. Note that the model does not account for host galaxy extinction.

(Tanvir et al. 2013; Abbott et al. 2017a)—when the relatively brighter afterglow has subsided. This emission has been attributed to a kilonova (Metzger et al. 2010; Roberts et al. 2011)—a type of emission powered by the radioactive decay of the heavy elements formed after the dynamically ejected and wind-driven neutron-rich material of the merger expands from nuclear densities and neutrons are captured via the r process. Predictions are that an ultraviolet kilonova precursor could also be detected from the decay of free neutrons in the fast material (Metzger et al. 2015). However, the short timescales of the GRB 180618A optical emission do not support r -process models, for which we also expect lower peak luminosities ($L_{\text{th}} = 10^{40}\text{--}10^{42}$ erg s^{-1} ; Metzger et al. 2010, 2015) than those estimated in GRB 180618A, i.e., $L_{\text{th}}(z = 0.554) \approx 2 \times 10^{45}$ erg s^{-1} .

We also discard thermal emission powered by the GRB jet. The measured luminosities and effective temperatures do not follow the scalings expected from thermal emission of the relativistic and nonrelativistic material of the jet cocoon (Nakar & Piran 2017; De Colle et al. 2018). Similarly, maximizing the signal from the jet cocoon at $z = 0.554$ corresponds to a very energetic long GRB and large energy stored in the jet cocoon, on the order of $E_c \approx 10^{52}$ erg (Nakar & Piran 2017). This would be expected to produce at most a ≈ 22 mag near-ultraviolet and ≈ 23.6 mag optical thermal rebrightening. These values are not consistent with the observed peak luminosities of the thermal emission (e.g., ≈ 18 mag in the UVOT $uvw1$ band, and ≈ 18.7 mag in the RINGO3 BV band), and they are far below the limiting magnitude of our UVOT and RINGO3 observations. Furthermore, successful jets in energetic engines like GRB 180618A are expected to have an early breakout from the stellar envelope, which cuts thermalization and leads to most of the jet energy leaving the ejecta (Ramirez-Ruiz et al. 2002; Duffell et al. 2018; Izzo et al. 2019).

4.2. Thermal Emission from a Relativistically Expanding Magnetar Wind Nebula

Here, we explore the possibility that the observed thermal emission from GRB 180618A could be explained by a magnetar wind nebula (Yu et al. 2013; Metzger & Piro 2014;

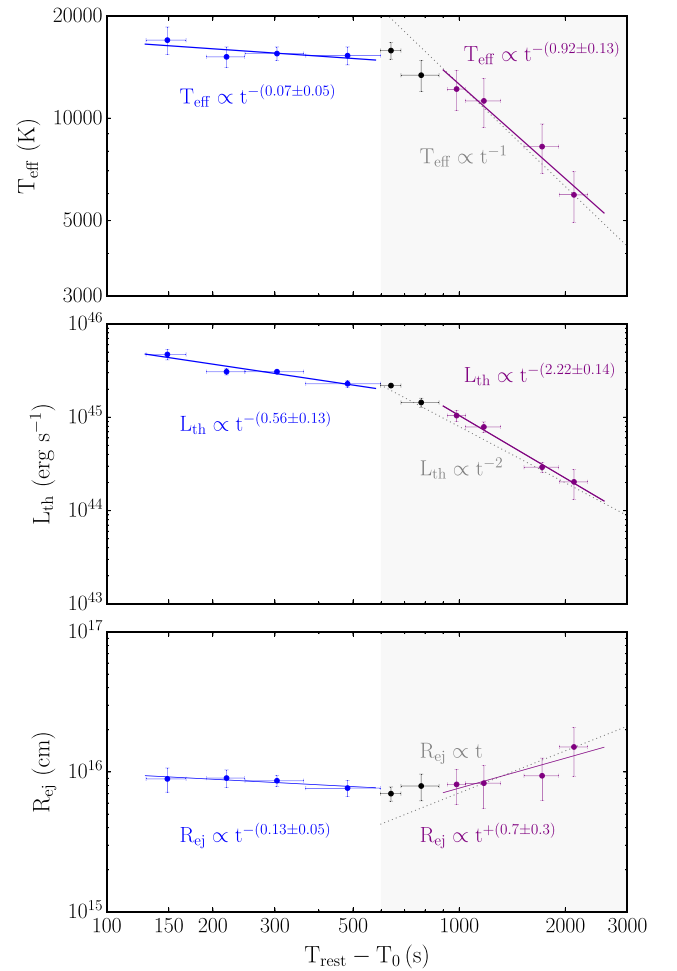


Figure 12. Temporal evolution of the effective temperatures (T_{eff}), luminosities (L_{th}), and photospheric radii (R_{ej}) of the best-fitting blackbody models at the host galaxy rest frame (i.e., $z = 0.554$). The shaded gray area corresponds to the thermal contribution from the magnetar wind nebula, and the dotted gray line is the expected evolution of the temperature, luminosity, and radius for an optically thin regime.

Gao et al. 2015; Wollaeger et al. 2019) and the implications of such a model for this system.

In a magnetar wind nebula, the expanding ejecta shell is continually being heated from behind by the magnetar winds—a scenario that differs from fireball models with energy injection at a single point in time (e.g., Mészáros & Rees 1997; Nakar & Piran 2017). As such, the thermal luminosity is expected to track the spin-down luminosity of the magnetar as $L_{\text{th}} \propto L_{\text{sd}} \propto t^{-2}$ (Yu et al. 2013; Metzger & Piro 2014). Assuming that the ejecta radially expands as $R_{\text{ej}} \propto t$, the effective temperatures are expected to follow $T_{\text{eff}} = [L_{\text{th}} / (4\pi\sigma_{\text{B}}R_{\text{ej}}^2)]^{1/4} \propto L_{\text{th}}^{1/4} t^{-1/2} \propto t^{-1}$, where σ_{B} is the Stefan-Boltzmann constant.

In Figure 12, we model the temporal evolution of the best-fitting effective temperatures, luminosities, and photospheric radii (R_{ej}) with power laws. For data ≈ 1400 s post-burst, we find that the observed scalings $L_{\text{th}} \propto t^{-(2.22 \pm 0.14)}$, $T_{\text{eff}} \propto t^{-(0.92 \pm 0.13)}$, and $R_{\text{ej}} \propto t^{+(0.7 \pm 0.3)}$ are compatible with those expected in a magnetar nebula (Metzger & Piro 2014). The peak luminosity $L_{\text{th}}(z = 0.554) \approx 2 \times 10^{45}$ erg s^{-1} of GRB 180618A is also within the expected values (Yu et al. 2013; Metzger & Piro 2014). Note that data 900–1400 s post-burst are

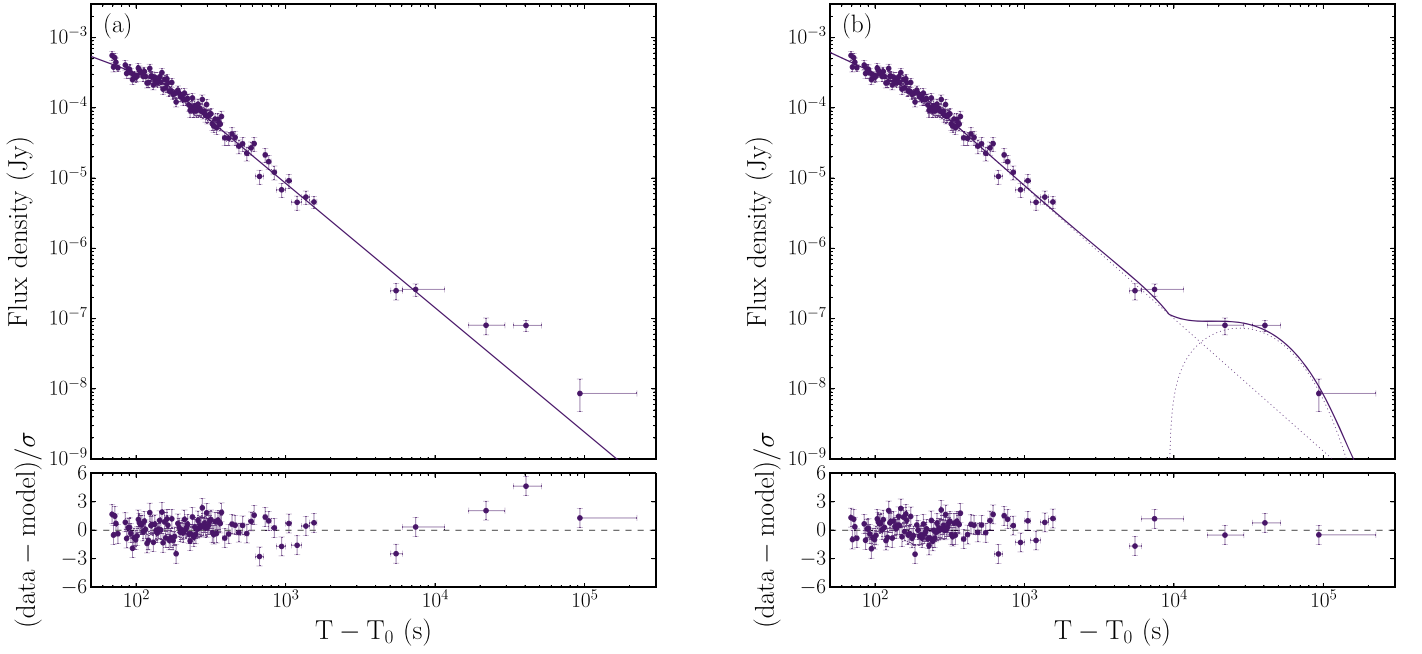


Figure 13. Best-fitting models of the XRT X-ray light curve of GRB 180618A. (a) Broken power-law model. The best-fitting parameters are an initial decay rate of $\alpha_{X,1} = 0.79 \pm 0.12$, steeping to $\alpha_{X,2} = 1.77 \pm 0.04$ at $t_{\text{break}} = 162 \pm 11$ s ($\chi^2/\text{dof} = 131/102$). (b) Broken power-law model plus a pulse function, with $\alpha_{X,1} = 0.99 \pm 0.07$, $\alpha_{X,2} = 1.89 \pm 0.06$, $t_{\text{break}} = 206 \pm 14$ s ($\chi^2/\text{dof} = 104/99$). The bottom panels are the residuals of the best-fitting model.

still in agreement with the model, and that the deviation we detect is likely due to the contribution from the external shock, which dominates the emission before 900 s post-burst (see Section 4.4).

A newborn millisecond magnetar from a binary neutron star merger is expected to be close to the centrifugal breakup limit (Giacomazzo & Perna 2013; Fryer et al. 2015), with an initial spin period of $P_i \approx 1$ ms. Consequently, ejecta below a critical mass $M_{\text{ej}} \approx 10^{-2} M_{\odot} P_i^{-2}$ can be accelerated to transrelativistic speeds ($\Gamma \geq 1$) by the magnetar wind (Gao et al. 2013; Yu et al. 2013), where $\Gamma = (1 - \beta^2)^{-1/2}$ is the Lorentz factor, and $\beta = v/c$ is the ratio of the velocity between the inertial reference frames and the speed of light in vacuum. From the photospheric radius of the best-fitting blackbody model at the engine rest frame, $R'_{\text{ej}} = ct' \approx ct_{\text{obs}}(1+z)^{-1}(1-\beta)^{-1} \approx 2\Gamma^2 ct_{\text{obs}}(1+z)^{-1}$, we find that the ejecta in the GRB 180618A system is expanding at mildly relativistic speeds, i.e., $\Gamma(z = 0.554) \approx 9$.

For such low ejecta masses giving rise to high Lorentz factors, the ejecta can become optically thin before the diffusion time (Yu et al. 2013), i.e., when the optical depth $\tau' = (3M_{\text{ej}}\kappa)/(4\pi R'^2) \approx 1$, where κ is the opacity and M_{ej} is the isotropic-equivalent mass of the ejecta. The optical depth can be significantly raised (for a total mass in the shell) given electron-positron pair creation in the region behind the ejecta shell (Metzger & Piro 2014). We estimate the maximum pair multiplicity by assuming that a fraction ≈ 0.1 of the magnetar rotational energy $E_{\text{rot}} \approx 10^{52}$ erg is converted through a pair cascade process into electron-positron pairs in the nebula (Metzger & Piro 2014), such that $\kappa_{\pm} \approx (0.1E_{\text{rot}}/m_e c^2)(m_p/M_{\text{ej}}) \approx 10^3(M_{\text{ej}}/10^{-3}M_{\odot})^{-1}$. That is, pairs contribute $\approx 10^3$ times to the opacity for their mass than an electron-ion outflow, with a typical electron-scattering opacity of $\kappa \approx 0.2 \text{ cm}^2 \text{ g}^{-1}$ (Yu et al. 2013; Metzger et al. 2015). Given an electron-positron annihilation rate slower than the outflow expansion speed at late times (Metzger & Piro 2014), the pair opacity will still dominate the total opacity by the time of observations. Therefore, assuming an optically thin regime

($\tau' \lesssim 1$) when we start to notice the thermal emission ($t_{\text{obs}} \lesssim 10^3$ s) and opacity $\kappa \approx (0.2 \text{ cm}^2 \text{ g}^{-1})\kappa_{\pm}$, we estimate ejecta masses $M_{\text{ej}} \lesssim 10^{-4} M_{\odot} (\kappa_{\pm}/10^3)^{-1}$ at the polar regions of the system. This is consistent with the mass loss expected from merger remnants (e.g., Oechslin & Janka 2006; Lee & Ramirez-Ruiz 2007).

4.3. Nonthermal Emission from a Magnetar Wind Nebula

We used the GRB 180618A pipeline-processed products of the Swift XRT (Burrows et al. 2005; Evans et al. 2009), and we modeled the 0.3–10 keV light curve with a broken power-law function (see Figure 13(a)). We find a significant emission excess of 4.6σ at $t \approx 4 \times 10^4$ s post-burst, which we modeled with a pulse function (Piranomonte et al. 2008), i.e., $F = F_0(t - t_0)e^{-(t-t_0)/\tau_{\sigma}}$. The best-fitting parameters of this model are an initial emission decay rate of $\alpha_{X,1} = 0.99 \pm 0.07$ and a break at $t_{\text{break}} = 206 \pm 14$ s post-burst followed by a steeper decay with $\alpha_{X,2} = 1.89 \pm 0.06$ (see Figure 13(b)). For the late-time rebrightening, we find $t_0 = (9.3 \pm 3.8) \times 10^3$ s and $\tau_{\sigma} = (1.8 \pm 0.3) \times 10^4$ s.

If the magnetar winds are powerful enough and the ejecta mass is low, the nebula can be fully ionized at late times and X-ray emission will be able to leak out the nebula (Metzger & Piro 2014; Gao et al. 2015). This is consistent with the X-ray late-time rebrightening of GRB 180618A and implies that we are directly detecting the magnetar spin-down luminosity. This emission is expected to follow $L_{\text{sd}} = L_0(1 + t/t_{\text{sd}})^{-2}$ with typical values $L_0 = 1.7 \times 10^{50} B_{15}^2 P_{i,-3}^{-4}$ erg s $^{-1}$ and $t_{\text{sd}} = 307 B_{15}^{-2} P_{i,-3}^2$ s (e.g., Metzger 2019), which correspond to a cooled neutron star of 12 km fiducial radius (Beznogov et al. 2020), magnetic field $B_{15} \approx 10^{15}$ G, and initial spin $P_{i,-3} \approx 1$ ms (see, e.g., Rosswog et al. 2003).

At early times ($t \ll t_{\text{sd}}$), the luminosity of the magnetar from GRB 180618A is estimated to be $L_0 \approx L_{\text{iso}} f_b / \eta$, where $f_b \approx \theta_{\text{j,EE}}^2 / 2$ is the beaming factor, η is the radiative efficiency,

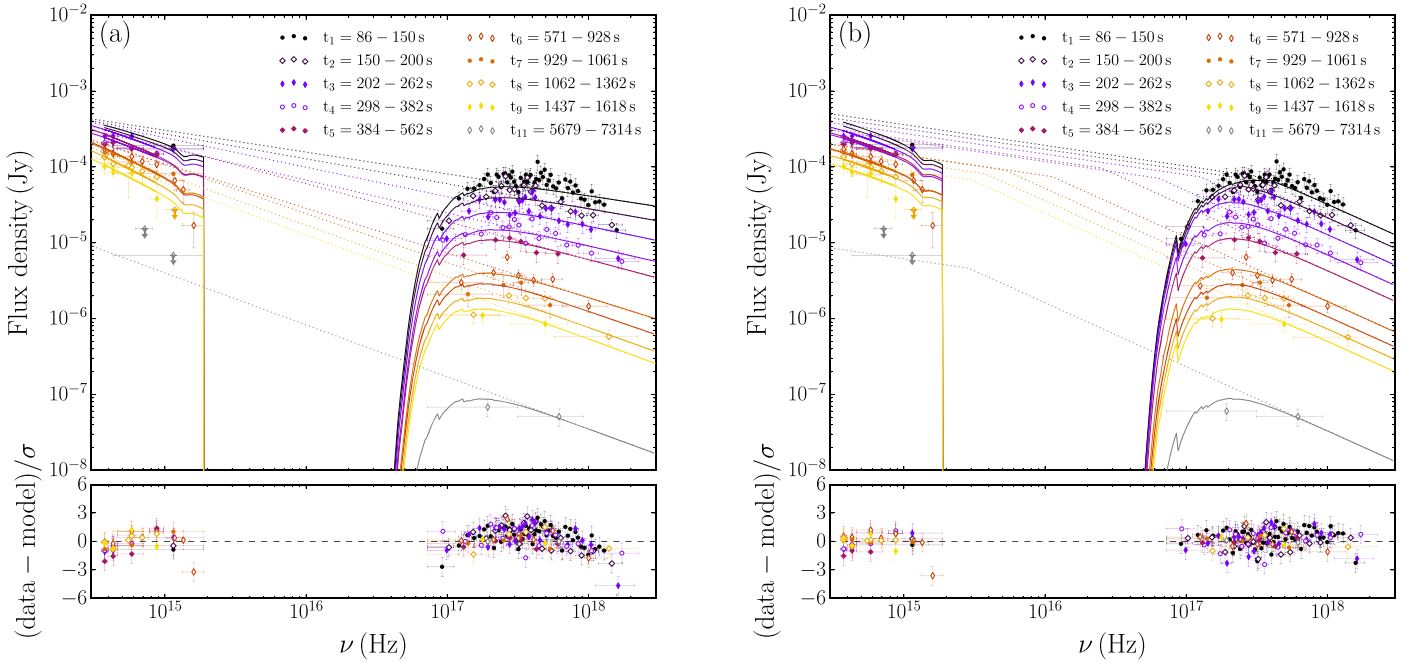


Figure 14. Spectral energy distributions of the co-temporal X-ray, optical, and ultraviolet observations of GRB 180618A. The XRT, UVOT, and RINGO3 data are modeled with the following synchrotron models. (a) Power laws ($\chi^2/\text{dof} = 292/159$). (b) Broken power laws with a joint optical and X-ray spectral indexes ($\chi^2/\text{dof} = 170/158$). The best-fitting spectral indexes are $\beta_{\text{opt}} = 0.27 \pm 0.02$ and $\beta_X = 0.84 \pm 0.05$. Note that we have fixed the break of the t_{11} epoch (gray color) to the t_{10} epoch value given the optical upper limits. In dotted lines, we show the best-fitting synchrotron model and in solid lines the model that includes the dust and hydrogen absorption from the Milky Way and host galaxy for a redshift $z = 0.554$. Detections have 1σ error bars, and nondetections are presented as 3σ upper limits.

and $\theta_{j,EE}$ is the jet opening angle. For a redshift $z = 0.554$ and assuming a large opening angle for the magnetar wind (i.e., $f_b/\eta \approx 1$; Bucciantini et al. 2012), the characteristic luminosity is $L_0(z = 0.554) \approx 2 \times 10^{49} \text{ erg s}^{-1}$. Furthermore, for a rebrightening of $L_X(z = 0.554) \approx 4 \times 10^{44} \text{ erg s}^{-1}$ at $t \approx 5 \times 10^4 (1+z)^{-1} \text{ s}$ post-burst, the characteristic spin-down time of the magnetar needs to be $t_{\text{sd}} \approx 200(1+z)^{-1} \text{ s}$. Note that this is consistent with the early optical plateau of the UVOT *white* band that we detect with a decay rate of $\alpha_{\text{opt,white}} = 0.12 \pm 0.08$ at $t \lesssim 200 \text{ s}$ post-burst (see also Rowlinson et al. 2013; Knust et al. 2017). Given all these constraints, we estimate the initial spin of the magnetar remnant of GRB 180618A to be $P_i \approx 4 \text{ ms}$, with a magnetic field of $B \approx 6 \times 10^{15} \text{ G}$.

In the magnetar scenario, a multiwavelength rebrightening could also be detectable hours to days post-burst given the deceleration of the mildly relativistic ejecta by the circumburst medium (Gao et al. 2013). At redshift $z = 0.554$, testing this prediction would have required sensitive late-time observations (e.g., Perley et al. 2009). That is, given typical values of the circumburst medium for a $\approx 10 \text{ kpc}$ GRB–host galaxy offset ($n \lesssim 10^{-3} \text{ cm}^{-3}$; Fong et al. 2015), the best-case scenario for GRB 180618A corresponds to an emission excess with peak luminosity $\lesssim 10^{-9} \text{ Jy}$ at X-ray bands, $\lesssim 25 \text{ mag}$ at optical bands, and $\lesssim 100 \mu\text{Jy}$ at radio bands (Gao et al. 2013).

4.4. Nonthermal Emission from the Afterglow

The deceleration of the relativistic ejecta by the circumburst medium should also have left an early imprint on the overall emission. To reproduce the synchrotron spectrum of this external shock (Piran 1999), we modeled the joint optical and X-ray spectral energy distributions with absorbed power laws and broken power laws in Xspec (see Figures 14(a), (b)). Given the spectral slopes and the progression of the break to lower

frequencies, we find that there must be at least one break frequency in between the bands and that it must be either the synchrotron or cooling frequency in an interstellar medium (Chevalier & Li 2000).

For the data after the X-ray light-curve break and the optical plateau, we tried two physical models for the GRB synchrotron spectrum: the fast and slow cooling of the electrons (e.g., Piran 1999). The best-fitting synchrotron models display trends in the residuals and suggest an additional spectral component at optical bands (see Figures 15(a), (b)). Therefore, having in mind the findings in Section 4.2, we introduced a blackbody profile in the model (see Figures 15(c), (d)). The best-fitting synchrotron plus blackbody model suggests a synchrotron spectrum with a rather hard electron index ($p = 1.6 \pm 0.1$ with spectral slopes $\beta_{\text{opt}} = \beta_{\text{opt,PI}} - 1 = 0.30 \pm 0.06$ and $\beta_X = \beta_{\text{opt}} + 0.5$), an interstellar medium profile, a slow-cooling regime, the cooling frequency in between the optical and X-ray bands, a blackbody profile contributing from $\approx 900 \text{ s}$ post-burst, and low host galaxy dust extinction, i.e., $E(B - V)_{\text{HG}} < 0.02$ —consistent with the GRB 180618A–host galaxy large offset. Additionally, we note that the constraint on polarization of $P_{\text{BV}} < 6.1\%$ at early times supports the scenario of unpolarized forward shocks in short GRBs (see, e.g., Jordana-Mitjans et al. 2021 for long GRBs).

This physical model suggests that when the thermal emission subsides, we should detect the underlying afterglow again. Around 3300 s post-burst, the fast-fading afterglow emission should be $F_\nu \approx 7 \times 10^{-6} \text{ Jy}$, which we speculate that it is consistent with the subtle light-curve flattening of the RINGO3 *BV* band, with $F_\nu = (9 \pm 3) \times 10^{-6} \text{ Jy}$. Furthermore, the emission across the optical and X-ray bands is decaying faster than expected for spherical expansion (Racusin et al. 2009) and suggests a collimated relativistic outflow.

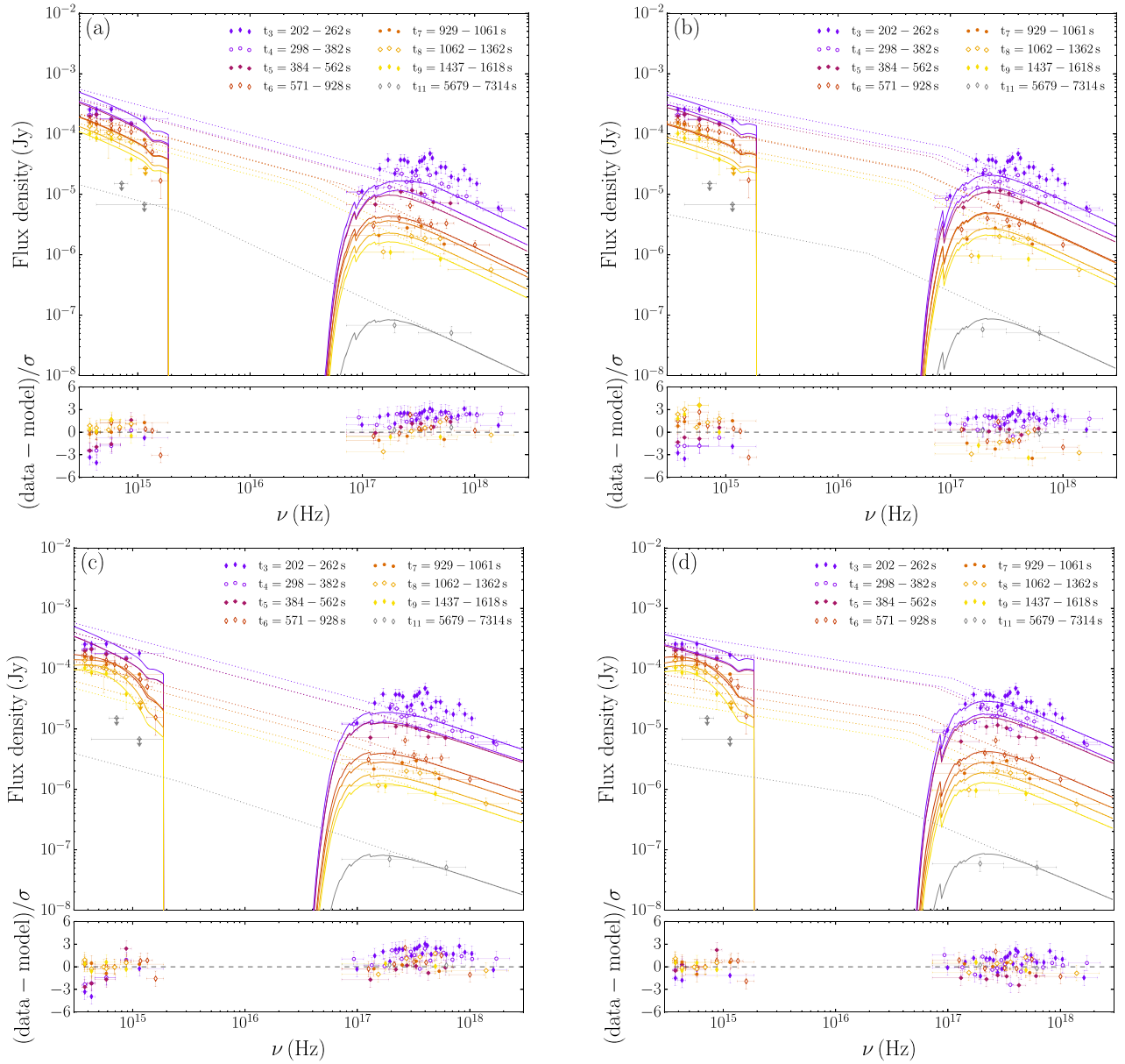


Figure 15. Spectral energy distributions of the co-temporal X-ray, optical, and ultraviolet observations of GRB 180618A. The data after the *white-band* UVOT plateau (i.e., $\gtrsim 200$ s post-burst) are modeled with the following physical models. (a) Fast cooling of the electrons ($\chi^2/\text{dof} = 309/90$). That is, we fix the optical spectral index to $\beta_{\text{opt}} = \beta_{\text{opt,PI}} - 1 = 0.5$, and we let the synchrotron frequency evolve as $\nu_m \propto t^{-1.5}$. (b) Slow cooling of the electrons ($\chi^2/\text{dof} = 330/90$), i.e., we fix $\beta_X = \beta_{\text{opt}} + 0.5$ and the cooling frequency $\nu_c \propto t^{-0.5}$. (c) Fast cooling and a blackbody profile ($\chi^2/\text{dof} = 231/82$). (d) Slow cooling and a blackbody profile ($\chi^2/\text{dof} = 106/82$). The best-fitting optical spectral index is $\beta_{\text{opt}} = 0.30 \pm 0.08$ ($\beta_X = \beta_{\text{opt}} + 0.5$), which corresponds to an electron index $p = 1.6 \pm 0.1$. The dust contribution from the host galaxy is estimated to be $E(B - V)_{\text{HG}} < 0.02$.

4.5. A Collimated Outflow

The temporal and spectral properties of the early X-ray emission of GRB 180618A satisfy closure relations for a jetted outflow with a hard electron index. That is, the first light-curve segment corresponds to the normal spherical decay rate of the afterglow (with average $\alpha_X \approx 1.2$) and the second segment to the post-jet-break decay ($\alpha_X \approx 2$; Racusin et al. 2009). For an interstellar medium profile, a slow-cooling regime, and with the X-ray band above the cooling frequency, a mean spectral index of $\beta_X = 0.80 \pm 0.06$ implies an electron index of $p = 1.6 \pm 0.1$; see also the temporal evolution of β_X in Figure 2 (bottom panel). We find a temporal slope of $\alpha_{X,1} = (3\beta_X + 5)/8 = 0.93 \pm 0.02$ for the normal spherical decay of

the afterglow and $\alpha_{X,2} = (\beta_X + 3)/2 = 1.90 \pm 0.03$ after the light-curve jet break, for an uniform jet scenario with lateral spreading (Zhang & Mészáros 2004; Racusin et al. 2009)—consistent with the observed decay rates of the X-ray light curve. Accounting for the early jet break at $t \approx 200$ s post-burst (Sari et al. 1999) and the fact that we are detecting the bright gamma-ray prompt emission (Yamazaki et al. 2002), we suggest that the observer faces the jet with a line of sight that likely runs near the jet edge. Overall, GRB 180618A suggests that the degree of collimation (Fong et al. 2015) and the observer viewing angle are key in detecting the short-lived optical thermal emission (and the late-time X-ray rebrightening) in short GRBs.

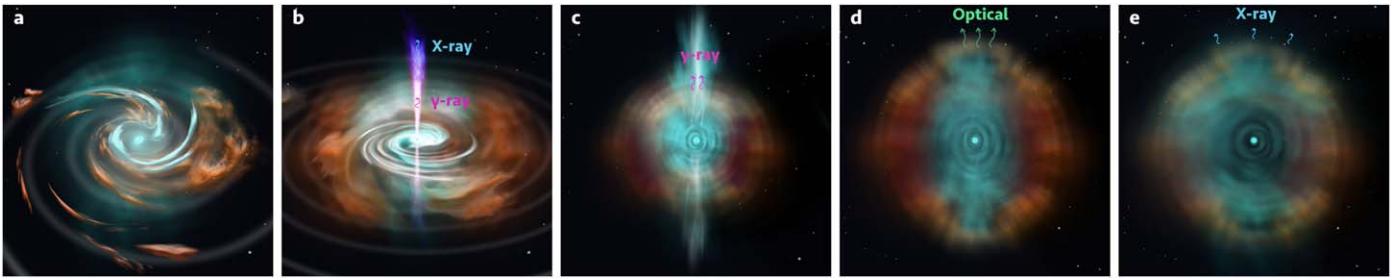


Figure 16. Artist impression of the different energy sources powering the GRB 180618A multiwavelength emission. (a) The material is equatorially ejected by tidal forces during the neutron star binary merger (Cucchiara et al. 2011) and radially ejected by hydrodynamic interactions at the neutron stars contact region (e.g., Metzger 2019). (b) The accretion of the torus onto a rotationally supported supramassive neutron star remnant (i.e., a millisecond magnetar) powers two relativistic jetted outflows (Bucciantini et al. 2012; Metzger et al. 2018) that, via internal dissipation mechanisms, produce the initial ≈ 0.3 s hard prompt gamma-ray emission. At this stage, the accretion disk releases winds that largely dominate the total mass ejected (Margalit & Metzger 2019). (c) The winds from the rotationally powered magnetar are collimated by the surrounding ejecta, which give rise to the ≈ 45 s duration soft gamma-ray emission (Bucciantini et al. 2012). (d) As the spin-down luminosity of the magnetar decreases, the jetted winds become stifled behind the ejecta, which is reheated at larger radii. When the opacity of the ejecta decreases sufficiently, bright optical thermal emission is emitted (Yu et al. 2013; Metzger & Piro 2014; Metzger 2019). (e) Hours after the merger, the ejecta is fully ionized by the winds of the long-lived magnetar, and the magnetar spin-down luminosity is detected (Metzger & Piro 2014).

5. Discussion

The early-time multiwavelength observations of short GRB 180618A propose a scenario in which only a long-lived magnetar remnant can account for all the observed emission components (see Figure 16): the extended soft gamma-ray emission following the short GRB (Metzger et al. 2008; Bucciantini et al. 2012), the unusual optical light curve (Yu et al. 2013; Metzger & Piro 2014), and the additional X-ray component (Metzger & Piro 2014; Gao et al. 2015).

Tens of magnetars have been identified in our Galaxy so far (Kaspi & Beloborodov 2017), and some of them are regular X-ray bursters that, less frequently, emit at soft gamma-ray bands (Ridnaia et al. 2021). More recently, giant flares from extragalactic magnetars have also been associated with low-luminosity short-duration GRBs (Svinkin et al. 2021). However, the remnant of a neutron star binary merger is expected to be the more energetic version of a magnetar, a millisecond protomagnetar (Metzger & Piro 2014), which is rotationally powered with typical energies $E_{\text{rot}} \approx 10^{51} - 10^{53}$ erg, and will spin down until its collapse into a black hole (Margalit & Metzger 2019).

After a neutron star binary merger, if a newborn rapidly spinning magnetar has sufficient spin-down luminosity, the winds will pierce through the ejecta and be collimated into bipolar jetted outflows that will dissipate Poynting-flux energy—powering the extended gamma-ray emission of GRB 180618A (Metzger et al. 2008; Bucciantini et al. 2012). As the spin-down luminosity of the magnetar decreases with $L_{\text{sd}} \propto t^{-2}$, these winds are trapped behind the ejecta forming a hot nebula of electron–positron pairs that will radiate via synchrotron and inverse Compton emission (Metzger & Piro 2014). A fraction of the X-ray emission is then absorbed by the neutral ejecta walls and reprocessed into optical and infrared photons that are able to escape when the optical depth of the expanding ejecta decreases enough. This allows the magnetar-powered kilonova of GRB 180618A to be a hundred times brighter than a radioactively powered kilonova (Yu et al. 2013; Metzger & Piro 2014). Hours to days after the burst, if the strong magnetar winds can completely ionize the ejecta, nonthermal X-ray emission will leak from the nebula producing an X-ray excess (Metzger & Piro 2014), similar to that observed ≈ 0.5 days after GRB 180618A.

Our multiwavelength data also gives information about the geometry of the system. Given that we are detecting prompt gamma-ray emission that is bright and spectrally hard, we are likely facing the GRB jet (Yamazaki et al. 2002). If the magnetar is releasing energy and accelerating ejecta along the polar regions of the system, material can easily reach transrelativistic speeds (Metzger et al. 2008; Bucciantini et al. 2012). This extra kinetic energy is consistent with what we observe at optical bands; there is an early and rapid evolution of the thermal luminosity given the relativistically expanding photospheric radius and the fast-fading spin-down luminosity of the magnetar, which we measure as $L_{\text{th}} \propto t^{-(2.22 \pm 0.14)}$. For the optical to be reprocessed within the observed timescales, we require an ejecta mass $M_{\text{ej}} \lesssim 10^{-4} M_{\odot} (\kappa_{\pm}/10^3)^{-1}$ at the polar regions of the merger, which is reasonable given that a total ejected mass $\approx (0.01 - 0.3) M_{\odot}$ is expected in all directions (Oechslin & Janka 2006; Murguía-Berthier et al. 2017). This suggests that the merger ejecta distribution is considerably asymmetric, likely due to long-lasting cavities drilled by the early relativistic outflows or the disk winds ejecting more material in equatorial directions (Bucciantini et al. 2012).

Current magnetohydrodynamic simulations cannot form jetted outflows just from the neutron star binary merger itself (Ruiz & Shapiro 2017); successful jets require the formation and delayed collapse within a hundred milliseconds of an intermediate hypermassive neutron star (Murguía-Berthier et al. 2014). However, constraints on the nuclear equation of state suggest that 18%–65% of the neutron stars binary mergers will result in a less massive and rotationally supported supramassive neutron star remnant with longer lifetime (Fryer et al. 2015; Margalit & Metzger 2019). Without the need for the neutron star remnant to collapse into a black hole, a viable short GRB from a merger could be powered by direct accretion onto the magnetar (Bucciantini et al. 2012), or by the enhancement of the spin-down luminosity given the temporary presence of the accretion disk (Metzger et al. 2018). Yet, baryon pollution remains a concern in these environments (Lee & Ramirez-Ruiz 2007; Murguía-Berthier et al. 2014).

The multiwavelength data set of GRB 180618A confirms GW170817/GRB 170817A findings (Abbott et al. 2017b)—i.e., neutron star binaries as progenitors of short GRBs. While the remnant of gravitational wave event GW170817 is likely a hypermassive neutron star that collapsed into a black hole within the first few hundreds of milliseconds after the merger

(Abbott et al. 2017b; Metzger 2019), observations of short GRB 180618A suggest a different outcome. We observe that a vast energy reservoir is injected into the system on timescales much larger than the duration of the accretion disk outflows—powering several emission components across the spectrum that can only be explained by a long-lived magnetar remnant. Furthermore, it suggests that supramassive neutron stars with delayed collapse into a black hole are remnants of neutron star binary mergers (Fryer et al. 2015; Margalit & Metzger 2019), and can power short hard GRBs and extended soft gamma-ray emission through accretion and spin-down luminosity (Metzger et al. 2008; Bucciantini et al. 2012). These findings preserve a good agreement between the percentage of short GRBs that have extended emission (13%–50%; Norris et al. 2010; Lien et al. 2016), and the expected number of remnants from neutron star binary mergers that can power such emission (18%–65%; Margalit & Metzger 2019).

Future early-time studies of short GRBs with extended gamma-ray emission and joint GW/GRB detections will be able to statistically constrain how long and how many of these cosmological magnetars survive the merger, characterize the asymmetries in the distribution of the ejected mass, and probe jet acceleration in millisecond magnetars.

6. Conclusions

We report the multiwavelength observations of short GRB 180618A; a GRB with unique gamma-ray, X-ray, and optical properties result of a compact object binary merger at the outskirts of a galaxy at redshift $z = 0.554 \pm 0.001$.

The bright prompt gamma-ray emission of GRB 180618A consists of a multi-peaked structure with total duration ≈ 0.3 s and maximum energy radiated in the MeV domain, making GRB 180618A one of the most energetic gamma-ray pulses ever detected among short-duration GRBs (i.e., flux, fluence, E_{peak}). After the typically short and spectrally hard gamma-ray pulse, we also detect a period of weak extended gamma-ray emission below ≈ 100 keV, lasting ≈ 45 s.

We find no detectable polarization at optical bands and a rate of change of the light that initially follows a power law $F_{\nu} \propto t^{-\alpha}$, with index $\alpha = 0.46 \pm 0.02$. The optical emission is surprisingly short-lived, and the slow decline is replaced by a sudden drop in brightness 35 minutes post-burst, steepening to $\alpha = 4.6 \pm 0.3$. The light-curve break progressively passes from the ultraviolet to near-infrared bands. Afterwards, there is no further detection of the optical transient at the GRB 180618A coordinates.

The GRB 180618A optical counterpart presents temporal and spectral properties that do not satisfy the characteristic scalings of the synchrotron spectrum of the GRB afterglow (Sari et al. 1998)—powered by the shock of the relativistic collimated ejecta with the circumburst medium. In contrast, the fast-fading X-ray emission is consistent with a decelerating jetted outflow and with an extra emission component ≈ 0.5 days post-burst. This leads us to consider two distinct mechanisms powering the X-ray and unusual optical emission.

The modeling of the overall emission suggests thermal-like emission from a relativistically expanding source dominating the optical emission ≈ 15 –60 minutes post-burst, which naturally accounts for the sharp chromatic drop of the optical emission at high-frequency wavelengths. Furthermore, the X-ray to optical emission before 15 minutes post-burst is consistent with the fast-fading jet afterglow.














We interpret the unusual spectral and temporal properties of GRB 180618A as evidence of a highly magnetized, spinning neutron star that survives for longer than $\approx 10^5$ s after the merger and spins down at a rate $L_{\text{th}} \propto t^{-(2.22 \pm 0.14)}$ powering a relativistically expanding hot thermal nebula in the process. Here, we confirm that newborn millisecond magnetars can power bright emission components across the electromagnetic spectrum that remain detectable at cosmological distances: i.e., the extended soft gamma-ray emission following some short GRBs (Metzger et al. 2008; Bucciantini et al. 2012), optical plateaus at early times (Knust et al. 2017), the fast-evolving bright thermal optical emission (Yu et al. 2013; Metzger & Piro 2014), and the late-time flattening of the X-ray light curve (Metzger & Piro 2014; Gao et al. 2015). The early afterglow emission drop and the short-lived thermal optical emission may explain why such thermal emission has not been detected yet in other short GRBs with extended emission; this discovery opens a new era for searches of gravitational wave counterparts with fast-cadence surveys.

We thank the anonymous referee for their constructive comments that improved the clarity and accuracy of the paper. The research leading to these results has received funding from the European Union’s Horizon 2020 Program under the AHEAD project (grant agreement 654215). N.J.-M. and C.G. M. acknowledge financial support from Mr. Jim Sherwin and Mrs. Hiroko Sherwin. C.M. acknowledges support from the Science and Technology Facilities Council and the UK Research and Innovation (ST/N001265/1). E.R.-R. is supported in part by NASA grant NNG17PX03C, NSF grant AST-1911206, AST-1852393, and AST-1615881, and the Heising-Simons Foundation. A.G. acknowledges the financial support from the Slovenian Research Agency (grants P1-0031, I0-0033, J1-8136, J1-2460). M.M. acknowledges financial support from the Italian Ministry of University and Research—Project Proposal CIR01_00010. We acknowledge A. Becker for taking the data, R.T. Gatto for useful discussions, and D. Paris for the help in the data reduction of the LBC. We thank E. Burns and D. Burrows for useful discussions.

Facilities: Swift (BAT, XRT, and UVOT), Fermi (GBM), Liverpool:2 m (RINGO3 and IO:O), LBT (LBC and MODS).

Software: Matplotlib (Hunter 2007), SciPy (Virtanen et al. 2020), PyFITS (Barrett & Bridgman 1999), Astropy (Astropy Collaboration et al. 2013, 2018), Astropy Photutils (Bradley et al. 2016), Astroalign (Beroiz et al. 2020), Xspec and PyXspec (v12.9.1; Arnaud 1996; Arnaud et al. 1999), HEASoft (v6.22.1; Blackburn 1995), RMFit (v4.3.2; Gamma-ray astronomy Group 2014).

ORCID iDs

N. Jordana-Mitjans  <https://orcid.org/0000-0002-5467-8277>
 C. G. Mundell  <https://orcid.org/0000-0003-2809-8743>
 C. Guidorzi  <https://orcid.org/0000-0001-6869-0835>
 R. J. Smith  <https://orcid.org/0000-0003-3434-1922>
 E. Ramírez-Ruiz  <https://orcid.org/0000-0003-2558-3102>
 B. D. Metzger  <https://orcid.org/0000-0002-4670-7509>
 S. Kobayashi  <https://orcid.org/0000-0001-7946-4200>
 A. Gomboc  <https://orcid.org/0000-0002-0908-914X>
 I. A. Steele  <https://orcid.org/0000-0001-8397-5759>
 M. Shrestha  <https://orcid.org/0000-0002-4022-1874>
 M. Marongiu  <https://orcid.org/0000-0002-5817-4009>
 A. Rossi  <https://orcid.org/0000-0002-8860-6538>
 B. Rothberg  <https://orcid.org/0000-0003-2283-2185>

References

- Abbott, B. P., Abbott, R., Abbott, T. D., et al. 2017a, *ApJL*, **848**, L12
- Abbott, B. P., Abbott, R., Abbott, T. D., et al. 2017b, *ApJL*, **848**, L13
- Alam, S., Albareti, F. D., Allende Prieto, C., et al. 2015, *ApJS*, **219**, 12
- Amati, L. 2006, *MNRAS*, **372**, 233
- Aptekar, R. L., Frederiks, D. D., Golenetskii, S. V., et al. 1995, *SSRv*, **71**, 265
- Arnaud, K., Dorman, B., & Gordon, C. 1999, XSPEC: An X-ray spectral fitting package, Astrophysics Source Code Library, ascl:9910.005
- Arnaud, K. A. 1996, in ASP Conf. Ser. 101, *Astronomical Data Analysis Software and Systems V*, ed. G. H. Jacoby & J. Barnes (San Francisco, CA: ASP), 17
- Arnold, D. M., Steele, I. A., Bates, S. D., Mottram, C. J., & Smith, R. J. 2012, *Proc. SPIE*, **8446**, 84462J
- Astropy Collaboration, Price-Whelan, A. M., Sipőcz, B. M., et al. 2018, *AJ*, **156**, 123
- Astropy Collaboration, Robitaille, T. P., Tollerud, E. J., et al. 2013, *A&A*, **558**, A33
- Barkov, M. V., & Pozanenko, A. S. 2011, *MNRAS*, **417**, 2161
- Barrett, P. E., & Bridgman, W. T. 1999, in ASP Conf. Ser. 172, *PyFITS*, a FITS Module for Python, ed. D. M. Mehringer, R. L. Plante, & D. A. Roberts (San Francisco, CA: ASP), 483
- Barthelmy, S. D., Barbier, L. M., Cummings, J. R., et al. 2005, *SSRv*, **120**, 143
- Behroozi, P. S., Ramirez-Ruiz, E., & Fryer, C. L. 2014, *ApJ*, **792**, 123
- Berger, E. 2010, *ApJ*, **722**, 1946
- Berger, E., Fong, W., & Chornock, R. 2013, *ApJL*, **774**, L23
- Berger, E., Price, P. A., Cenko, S. B., et al. 2005, *Natur*, **438**, 988
- Beroiz, M., Cabral, J. B., & Sanchez, B. 2020, *A&C*, **32**, 100384
- Beuermann, K., Hessman, F. V., Reinsch, K., et al. 1999, *A&A*, **352**, L26
- Beznogov, M. V., Page, D., & Ramirez-Ruiz, E. 2020, *ApJ*, **888**, 97
- Blackburn, J. K. 1995, in ASP Conf. Ser. 77, *FTOOLS: A FITS Data Processing and Analysis Software Package*, ed. R. A. Shaw, H. E. Payne, & J. J. E. Hayes (San Francisco, CA: ASP), 367
- Bloom, J. S., Frail, D. A., & Sari, R. 2001, *AJ*, **121**, 2879
- Bloom, J. S., Kulkarni, S. R., Djorgovski, S. G., et al. 1999, *Natur*, **401**, 453
- Bloom, J. S., Kulkarni, S. R., & Djorgovski, S. G. 2002, *AJ*, **123**, 1111
- Bradley, L., Sipocz, B., Robitaille, T., et al. 2016, *Photutils: Photometry tools*, Astrophysics Source Code Library, ascl:1609.011
- Breeveld, A. A., Landsman, W., Holland, S. T., et al. 2011, in AIP Conf. Proc. 1358, *Gamma Ray Bursts 2010*, ed. J. E. McEnery, J. L. Racusin, & N. Gehrels (Melville, NY: AIP), 373
- Bucciantini, N., Metzger, B. D., Thompson, T. A., & Quataert, E. 2012, *MNRAS*, **419**, 1537
- Burrows, D. N., Hill, J. E., Nousek, J. A., et al. 2005, *SSRv*, **120**, 165
- Calderone, G., Ghirlanda, G., Ghisellini, G., et al. 2015, *MNRAS*, **448**, 403
- Campana, S., Mangano, V., Blustin, A. J., et al. 2006, *Natur*, **442**, 1008
- Chevalier, R. A., & Li, Z.-Y. 2000, *ApJ*, **536**, 195
- Clarke, D., & Neumayer, D. 2002, *A&A*, **383**, 360
- Costa, E., Frontera, F., Heise, J., et al. 1997, *Natur*, **387**, 783
- Covino, S., Wiersema, K., Fan, Y. Z., et al. 2017, *NatAs*, **1**, 791
- Cucchiara, A., Levan, A. J., Fox, D. B., et al. 2011, *ApJ*, **736**, 7
- D'Avanzo, P., Salvaterra, R., Bernardini, M. G., et al. 2014, *MNRAS*, **442**, 2342
- De Colle, F., Lu, W., Kumar, P., Ramirez-Ruiz, E., & Smoot, G. 2018, *MNRAS*, **478**, 4553
- D'Elia, V., Campana, S., D'Ai, A., et al. 2018, *A&A*, **619**, A66
- Duffell, P. C., Quataert, E., Kasen, D., & Klion, H. 2018, *ApJ*, **866**, 3
- Evans, P. A., Beardmore, A. P., Page, K. L., et al. 2009, *MNRAS*, **397**, 1177
- Fermi-LAT Collaboration, Ajello, M., Atwood, W. B., et al. 2021, *NatAs*, **5**, 385
- Fong, W., & Berger, E. 2013, *ApJ*, **776**, 18
- Fong, W., Berger, E., Margutti, R., & Zauderer, B. A. 2015, *ApJ*, **815**, 102
- Fong, W.-f., Nugent, A. E., Dong, Y., et al. 2022, arXiv:2206.01763
- Fontana, A., Dunlop, J. S., Paris, D., et al. 2014, *A&A*, **570**, A11
- Fox, D. B., Frail, D. A., Price, P. A., et al. 2005, *Natur*, **437**, 845
- Fryer, C. L., Belczynski, K., Ramirez-Ruiz, E., et al. 2015, *ApJ*, **812**, 24
- Fryer, C. L., Woosley, S. E., Herant, M., & Davies, M. B. 1999, *ApJ*, **520**, 650
- Gamma-ray astronomy Group, U. o. A. H. 2014, *rmfit: Forward-folding spectral analysis software*, Astrophysics Source Code Library, ascl:1409.011
- Gao, H., Ding, X., Wu, X.-F., Dai, Z.-G., & Zhang, B. 2015, *ApJ*, **807**, 163
- Gao, H., Ding, X., Wu, X.-F., Zhang, B., & Dai, Z.-G. 2013, *ApJ*, **771**, 86
- Gehrels, N., Ramirez-Ruiz, E., & Fox, D. B. 2009, *ARA&A*, **47**, 567
- Ghirlanda, G., Nava, L., Ghisellini, G., Celotti, A., & Firmani, C. 2009, *A&A*, **496**, 585
- Giacomazzo, B., & Perna, R. 2013, *ApJL*, **771**, L26
- Giallongo, E., Ragazzoni, R., Grazian, A., et al. 2008, *A&A*, **482**, 349
- Goldstein, A., Veres, P., Burns, E., et al. 2017, *ApJL*, **848**, L14
- Guidorzi, C., Monfardini, A., Gomboc, A., et al. 2006, *PASP*, **118**, 288
- Guiriec, S., Briggs, M. S., Connaughton, V., et al. 2010, *ApJ*, **725**, 225
- Hamburg, R., Bissaldi, E., & Fermi GBM Team 2018, *GCN*, **22794**, 1
- Hill, J. M., Green, R. F., & Slagle, J. H. 2006, *Proc. SPIE*, **6267**, 62670Y
- Hjorth, J., Watson, D., Fynbo, J. P. U., et al. 2005, *Natur*, **437**, 859
- Høg, E., Fabricius, C., Makarov, V. V., et al. 2000, *A&A*, **355**, L27
- Hu, Y.-D., Liang, E.-W., Xi, S.-Q., et al. 2014, *ApJ*, **789**, 145
- Hunter, J. D. 2007, *CSE*, **9**, 90
- Izzo, L., de Ugarte Postigo, A., Maeda, K., et al. 2019, *Natur*, **565**, 324
- Jordana-Mitjans, N., Mundell, C. G., Kobayashi, S., et al. 2020, *ApJ*, **892**, 97
- Jordana-Mitjans, N., Mundell, C. G., Smith, R. J., et al. 2021, *MNRAS*, **505**, 2662
- Kaneko, Y., Bostanci, Z. F., Göğüş, E., & Lin, L. 2015, *MNRAS*, **452**, 824
- Kann, D. A., Klose, S., Zhang, B., et al. 2011, *ApJ*, **734**, 96
- Kaspi, V. M., & Beloborodov, A. M. 2017, *ARA&A*, **55**, 261
- Kelley, L. Z., Ramirez-Ruiz, E., Zemp, M., Diemand, J., & Mandel, I. 2010, *ApJL*, **725**, L91
- Knust, F., Greiner, J., van Eerten, H. J., et al. 2017, *A&A*, **607**, A84
- Kobayashi, S. 2000, *ApJ*, **545**, 807
- Kouveliotou, C., Meegan, C. A., Fishman, G. J., et al. 1993, *ApJL*, **413**, L101
- Krühler, T., Schady, P., Greiner, J., et al. 2011, *A&A*, **526**, A153
- LaPorte, S. J., Barthelmy, S. D., Kennea, J. A., et al. 2018, *GCN*, **22790**, 1
- Lee, W. H., & Ramirez-Ruiz, E. 2007, *NJPh*, **9**, 17
- Lee, W. H., Ramirez-Ruiz, E., & López-Cámara, D. 2009, *ApJL*, **699**, L93
- Lien, A., Sakamoto, T., Barthelmy, S. D., et al. 2016, *ApJ*, **829**, 7
- Liu, C., Zhang, Y., Li, X., et al. 2020, *SCPMA*, **63**, 249503
- MacFadyen, A. I., & Woosley, S. E. 1999, *ApJ*, **524**, 262
- Margalit, B., & Metzger, B. D. 2019, *ApJL*, **880**, L15
- Mazaeva, E., Kusakin, A., Pozanenko, A., et al. 2018, *GCN*, **22809**, 1
- Meegan, C., Lichti, G., Bhat, P. N., et al. 2009, *ApJ*, **702**, 791
- Mészáros, P., & Rees, M. J. 1997, *ApJ*, **476**, 232
- Metzger, B. D. 2019, *LRR*, **23**, 1
- Metzger, B. D., Bauswein, A., Goriely, S., & Kasen, D. 2015, *MNRAS*, **446**, 1115
- Metzger, B. D., Beniamini, P., & Giannios, D. 2018, *ApJ*, **857**, 95
- Metzger, B. D., Martínez-Pinedo, G., Darbha, S., et al. 2010, *MNRAS*, **406**, 2650
- Metzger, B. D., & Piro, A. L. 2014, *MNRAS*, **439**, 3916
- Metzger, B. D., Quataert, E., & Thompson, T. A. 2008, *MNRAS*, **385**, 1455
- Molinari, E., Vergani, S. D., Malesani, D., et al. 2007, *A&A*, **469**, L13
- Moss, M., Lien, A., Guiriec, S., Cenko, S. B., & Sakamoto, T. 2022, *ApJ*, **927**, 157
- Mösta, P., Radice, D., Haas, R., Schnetter, E., & Bernuzzi, S. 2020, *ApJL*, **901**, L37
- Mundell, C. G., Kopač, D., Arnold, D. M., et al. 2013, *Natur*, **504**, 119
- Murguía-Berthier, A., Montes, G., Ramirez-Ruiz, E., De Colle, F., & Lee, W. H. 2014, *ApJL*, **788**, L8
- Murguía-Berthier, A., Ramirez-Ruiz, E., De Colle, F., et al. 2021, *ApJ*, **908**, 152
- Murguía-Berthier, A., Ramirez-Ruiz, E., Montes, G., et al. 2017, *ApJL*, **835**, L34
- Nakar, E., & Piran, T. 2017, *ApJ*, **834**, 28
- Norris, J. P., & Bonnell, J. T. 2006, *ApJ*, **643**, 266
- Norris, J. P., Gehrels, N., & Scargle, J. D. 2010, *ApJ*, **717**, 411
- Nugent, A. E., Fong, W.-f., Dong, Y., et al. 2022, arXiv:2206.01764
- O'Connor, B., Troja, E., Dichiara, S., et al. 2022, *MNRAS*, **515**, 4890
- Oechslin, R., & Janka, H. T. 2006, *MNRAS*, **368**, 1489
- Paczynski, B. 1986, *ApJL*, **308**, L43
- Perley, D. A., Metzger, B. D., Granot, J., et al. 2009, *ApJ*, **696**, 1871
- Piran, T. 1999, *PhR*, **314**, 575
- Piranomonte, S., D'Avanzo, P., Covino, S., et al. 2008, *A&A*, **491**, 183
- Planck Collaboration, Aghanim, N., Akrami, Y., et al. 2020, *A&A*, **641**, A6
- Pogge, R. 2019, *rwpgogge/modsCCDRed: v2.0.1*, Zenodo, doi:10.5281/zenodo.2647501
- Pogge, R. W., Atwood, B., Brewer, D. F., et al. 2010, *Proc. SPIE*, **7735**, 77350A
- Poolakkil, S., Preece, R., Fletcher, C., et al. 2021, *ApJ*, **913**, 60
- Poole, T. S., Breeveld, A. A., Page, M. J., et al. 2008, *MNRAS*, **383**, 627
- Racusin, J. L., Liang, E. W., Burrows, D. N., et al. 2009, *ApJ*, **698**, 43
- Ragazzoni, R., Giallongo, E., Pasian, F., et al. 2000, *Proc. SPIE*, **4008**, 439
- Ramirez-Ruiz, E., Andrews, J. J., & Schröder, S. L. 2019, *ApJL*, **883**, L6
- Ramirez-Ruiz, E., Celotti, A., & Rees, M. J. 2002, *MNRAS*, **337**, 1349
- Rastinejad, J. C., Gompertz, B. P., Levan, A. J., et al. 2022, arXiv:2204.10864
- Rees, M. J., & Meszaros, P. 1992, *MNRAS*, **258**, 41P
- Ridnaia, A., Svinikin, D., Frederiks, D., et al. 2021, *NatAs*, **5**, 372

- Roberts, L. F., Kasen, D., Lee, W. H., & Ramirez-Ruiz, E. 2011, *ApJL*, **736**, L21
- Roberts, O. J., Veres, P., Baring, M. G., et al. 2021, *Natur*, **589**, 207
- Roming, P. W. A., Kennedy, T. E., Mason, K. O., et al. 2005, *SSRv*, **120**, 95
- Rosswog, S. 2007, *MNRAS Lett.*, **376**, L48
- Rosswog, S., Ramirez-Ruiz, E., & Davies, M. B. 2003, *MNRAS*, **345**, 1077
- Rowlinson, A., O'Brien, P. T., Metzger, B. D., Tanvir, N. R., & Levan, A. J. 2013, *MNRAS*, **430**, 1061
- Ruiz, M., & Shapiro, S. L. 2017, *PhRvD*, **96**, 084063
- Sakamoto, T., Barthelmy, S. D., Cummings, J. R., et al. 2018, GCN, **22796**, 1
- Sari, R. 1999, *ApJL*, **524**, L43
- Sari, R., & Piran, T. 1999, *ApJ*, **520**, 641
- Sari, R., Piran, T., & Halpern, J. P. 1999, *ApJL*, **519**, L17
- Sari, R., Piran, T., & Narayan, R. 1998, *ApJL*, **497**, L17
- Scargle, J. D. 1998, *ApJ*, **504**, 405
- Schlegel, D. J., Finkbeiner, D. P., & Davis, M. 1998, *ApJ*, **500**, 525
- Schmidt, G. D., Elston, R., & Lupie, O. L. 1992, *AJ*, **104**, 1563
- Sharma, V., Bhattacharya, D., Bhalerao, V., et al. 2018, GCN, **22842**, 1
- Siegel, M. H., LaPorte, S. J. & Swift/UVOT Team 2018, GCN, **22810**, 1
- Singh, K. P., Tandon, S. N., Agrawal, P. C., et al. 2014, *Proc. SPIE*, **9144**, 91441S
- Song, X.-Y., Xiong, S.-L., Zhang, S.-N., et al. 2022, *ApJS*, **259**, 46
- Steele, I. A. 2004, *AN*, **325**, 519
- Svinkin, D., Frederiks, D., Hurley, K., et al. 2021, *Natur*, **589**, 211
- Svinkin, D., Golenetskii, S., Aptekar, R., et al. 2018, GCN, **22822**, 1
- Tanvir, N. R., Levan, A. J., Fruchter, A. S., et al. 2013, *Natur*, **500**, 547
- Tanvir, N. R., Levan, A. J., González-Fernández, C., et al. 2017, *ApJL*, **848**, L27
- Thöne, C. C., de Ugarte Postigo, A., Fryer, C. L., et al. 2011, *Natur*, **480**, 72
- Tody, D. 1986, *Proc. SPIE*, **627**, 733
- Troja, E., Ryan, G., Piro, L., et al. 2018, *NatCo*, **9**, 4089
- Tsvetkova, A., Frederiks, D., Golenetskii, S., et al. 2017, *ApJ*, **850**, 161
- Tsvetkova, A., Frederiks, D., Svinkin, D., et al. 2021, *ApJ*, **908**, 83
- Turnshek, D. A., Bohlin, R. C., Williamson, R. L. I., et al. 1990, *AJ*, **99**, 1243
- Tyurina, N., Lipunov, V., Gorbvskoy, E., et al. 2018, GCN, **22797**, 1
- van Paradijs, J., Groot, P. J., Galama, T., et al. 1997, *Natur*, **386**, 686
- Villasenor, J. S., Lamb, D. Q., Ricker, G. R., et al. 2005, *Natur*, **437**, 855
- Virtanen, P., Gommers, R., Oliphant, T. E., et al. 2020, *NatMe*, **17**, 261
- von Kienlin, A., Meegan, C. A., Paciesas, W. S., et al. 2020, *ApJ*, **893**, 46
- Wollaeger, R. T., Fryer, C. L., Fontes, C. J., et al. 2019, *ApJ*, **880**, 22
- Woodsley, S. E. 1993, *ApJ*, **405**, 273
- Yamazaki, R., Ioka, K., & Nakamura, T. 2002, *ApJL*, **571**, L31
- Yu, Y.-W., Zhang, B., & Gao, H. 2013, *ApJL*, **776**, L40
- Zhang, B., Fan, Y. Z., Dyks, J., et al. 2006, *ApJ*, **642**, 354
- Zhang, B., & Mészáros, P. 2004, *IJMPA*, **19**, 2385
- Zhang, B., Zhang, B.-B., Virgili, F. J., et al. 2009, *ApJ*, **703**, 1696
- Zhang, B. B., Zhang, B., Sun, H., et al. 2018, *NatCo*, **9**, 447
- Zhang, H.-M., Liu, R.-Y., Zhong, S.-Q., & Wang, X.-Y. 2020, *ApJL*, **903**, L32
- Zhu, Z. P., Xu, D., Zhang, J. B., et al. 2018, GCN, **22804**, 1